Fast simulation of finite-beam optical coherence tomography of inhomogeneous turbid media

by

Micheal Sobhy

A thesis submitted to the Faculty of Graduate Studies of
the University of Manitoba,
in partial fulfillment of the requirements of the degree of

Master of Science

Biomedical Engineering
University of Manitoba
Winnipeg, Manitoba

ABSTRACT

We developed a fast simulator of finite-beam optical coherence tomography (OCT) of inhomogeneous turbid media. Our Sequential Monte Carlo (MC) based finite beam OCT simulator can reach more than a hundred times faster than one that represents a finite OCT's incident beam as a superposition of infinitely thin beams, i.e., a superposition-based MC simulator. In this thesis, first, we highlight the lesser-known correspondence between the commonly used MC simulation of light in turbid media, and Sequential MC based solution of the Radiative Transfer Equation (RTE). Second, we describe the implementation of our simulator of finite-beam OCT as a Sequential MC solution to the RTE. Third, we derive analytical expressions for the relationship between simulation errors and computational complexities, i.e., simulation times, for both our Sequential MC based simulator and a superposition-based MC simulator. We present simulation results of finite beam OCT of inhomogeneous turbid media when having a finite beam with a Gaussian intensity profile. Our simulator could be used in OCT design since it models realistic beam profiles that are typically used in OCT systems.

ACKNOWLEDGEMENTS

Deep thanks to the following persons.

- My advisor Prof. Sherif S. Sherif for his continuous guidance and support, it was a great opportunity to work under his supervision.
- My examination committee Prof. Stephen Pistorius, Prof. Ian Jeffrey, and Prof. Puyan Mojabi for their valuable feedback.
- My oral defense Chairperson Prof. Jayanne English for her time.
- All my family members, especially my father, mother, uncle, and wife, for their love, support, and encouragement.

TABLE OF CONTENTS

LIST OF FIGURES

LIST OF TABLES

Chapter 1

Introduction

Optical Coherence Tomography (OCT) is a relatively new imaging modality that was introduced in 1991 [1]. OCT has several advantages over other modalities, including: near histology level ($1 - 15\ \mu m$) imaging resolution, real-time image acquisition, and the use of non-ionizing radiation [1-5]. In addition, OCT could be coupled with endoscopy to image internal organs *in situ*, as it doesn't require optical coupling media [2, 4]. The applications of OCT in the biomedical field are increasing rapidly. Currently, OCT has applications in ophthalmology, cardiology, dermatology, oncology, dentistry, among others [4, 7].

Current OCT systems only consider single-scattered light for imaging, thereby limiting OCT imaging penetration depth to few millimeters from the surface [2, 4]. To overcome this limitation, we need to extract information from multiply scattered light, since it is dominant at higher depths. In order to do this, researchers need to understand more about light scattering in tissue and how multiple-scattered light contribute to the OCT signal. A realistic and fast simulator for OCT could help learn more about the contribution of multiply scattered light to the OCT signal. It is an important tool for OCT research, as it could help with the design of OCT imaging systems with higher penetration depth.

The current OCT simulators for inhomogeneous arbitrary-shaped turbid media assume that the incident light beam for imaging is infinitely-thin, i.e., infinitely small probing area. This is not a realistic assumption because the OCT signal will depend on the incident beam

diameter and intensity profile. Therefore, simulating a finite incident beam will make the simulation closer to reality. Typically, the signal due to a finite incident beam, i.e., finite probing area, could be approximated by repeating the simulation at a set of points covering the beam area then get the superposition of the results. But, this approach is computationally expensive, as it requires repeating the simulation of an infinitely-thin incident beam at each point (we will refer to this approach by the superposition approach). In this thesis, we focus on building a practical (fast) finite beam OCT simulator for inhomogeneous arbitrary-shaped turbid media.

1.1 Thesis Outline

To simulate OCT signals, we need to simulate light propagation in tissue. There are two approaches to model the propagation of light in turbid media, the electromagnetic (EM) approach that is based on Maxwell's equations, and the radiative transport (RT) approach that is based on the Radiative Transfer Equation (RTE). We review both approaches in Chapter 2 and highlight how the RTE is related to the Poynting theorem for energy conservation.

In Chapter 3, we briefly explain the theory of time-domain OCT and review the previous work on Monte Carlo time-domain OCT simulators. The main components of a massively parallel OCT simulator (OCT-MPS) for inhomogeneous arbitrarily shaped turbid media is reviewed, which we use as starting point to develop our finite beam simulator.

To simulate a finite incident beam in a practical way, we revisit the analytical solution of the RTE. In Chapter 4, we explain the basics of Monte Carlo (MC) quadrature methods, and how it could be used to solve Fredholm integral equations of the second kind. In

Chapter 5, we present a solution of the RTE for homogeneous media using MC quadrature methods, and show its equivalence to MC simulation of light.

Following the MC solution of the RTE, we consider including the incident beam as part of the simulation from the beginning, we will refer to this approach by the Sequential MC approach. In Chapter 6, we compare the error and computational cost of this Sequential MC approach to the traditional superposition approach. We chose the Sequential MC approach to build our finite beam OCT simulator because of its superior performance. We implemented our simulator on graphics processing units (GPUs) using the Compute Unified Device Architecture (CUDA) platform by NVIDIA® to exploit the parallelism inherent in the simulation. We also implemented a superposition-based simulator to validate the results of our simulator. We demonstrated the accuracy and speed of our simulator over the superposition-based simulator. We present simulated OCT reflectivity-based B-scan OCT images for two inhomogeneous arbitrarily shaped turbid media due a finite incident beam with a Gaussian intensity profile. Finally, in Chapter 7, we present our conclusions, and suggestions for future work.

1.2 Thesis research contributions

- We established the correspondence between the Sequential MC solution of the RTE for homogeneous media, written in the form of a Fredholm integral equation of the second type, with a common Monte Carlo light simulation procedure.
- We developed a fast simulator of finite-beam optical coherence tomography for inhomogeneous turbid media composed of arbitrarily shaped regions of different optical properties based on the Sequential MC solution of the RTE. We validated

our Sequential MC based simulator with one that represents the finite beam signal (A-scan) as the superposition of the signals (A-scans) due to infinitely-thin beams that cover the finite beam area, referred to by superposition-based simulator.

- We derived analytical expressions for the error in the estimates of our Sequential MC based simulator and the superposition-based simulator. We compared the errors of both simulator, and showed that the error of our simulator is always less than the error of the superposition-based simulator for a comparable computational cost.

Chapter 2

Light Propagation in Tissue

To simulate OCT signals from tissue, we need to understand how light propagates in tissue. Light is an electromagnetic (EM) radiation. As all EM radiations, light propagation is governed by Maxwell's equations [2, 8, 9]. One approach for finding the distribution of light in a medium is the EM approach, where one calculates the distribution of the electric and magnetic fields in a medium. The EM approach is easily applied to simple cases, e.g., layered media. However, in other cases such as tissue, where scattering and absorption take place in a complicated way, it becomes a challenging computational problem.

Another approach for finding the distribution of light in a medium is the Radiative Transfer (RT) approach. This approach considers only the energy of light rather than its EM field. Therefore it is relatively easier to obtain distributions of light in scattering media using this approach. The RT approach is commonly used to simulate light propagation for two main reasons. First, it simplifies the computational problem; second, in many problems, it is sufficient to simulate the intensity only. In this chapter, we will explain how both approaches model light propagation in tissue.

2.1 Electromagnetic approach for light propagation

Visible light occupies a band of relatively short wavelengths in the electromagnetic spectrum (between $400\,\text{nm}$ to $700\,\text{nm}$) [8]. The electromagnetic field constitutes two related fields, function of position and time: the electric field vector $\boldsymbol{E}(\boldsymbol{r}, t)$ and the magnetic field vector $\boldsymbol{H}(\boldsymbol{r}, t)$. James Clark Maxwell formulated a set of partial differential

equations that both the electric and magnetic fields must satisfy, known as Maxwell's equations [8, 10]. Before writing Maxwell's equations, we need to define two more vectors, the electric flux density $\boldsymbol{D}(\boldsymbol{r},t)$ and the magnetic flux density $\boldsymbol{B}(\boldsymbol{r},t)$. These vectors are used to describe the influence of the medium on the electric and magnetic fields [8, 10]. The electric flux density $\boldsymbol{D}(\boldsymbol{r},t)$ relates to the electric field $\boldsymbol{E}(\boldsymbol{r},t)$ and the magnetic flux density $\boldsymbol{B}(\boldsymbol{r},t)$ relates to the magnetic field $\boldsymbol{H}(\boldsymbol{r},t)$. Maxwell's equations, for a medium with continuous physical properties, are [11]:

$$\boldsymbol{\nabla} \times \boldsymbol{H}(\boldsymbol{r},t) - \frac{\partial \boldsymbol{D}(\boldsymbol{r},t)}{\partial t} = \boldsymbol{J}(\boldsymbol{r},t) \tag{2.1}$$

$$\boldsymbol{\nabla} \times \boldsymbol{E}(\boldsymbol{r},t) + \frac{\partial \boldsymbol{B}(\boldsymbol{r},t)}{\partial t} = 0 \tag{2.2}$$

$$\boldsymbol{\nabla} \cdot \boldsymbol{D}(\boldsymbol{r},t) = \rho(\boldsymbol{r},t) \tag{2.3}$$

$$\boldsymbol{\nabla} \cdot \boldsymbol{B}(\boldsymbol{r},t) = 0 \tag{2.4}$$

where, $\boldsymbol{J}(\boldsymbol{r},t)$ is the electric current density, and $\rho(\boldsymbol{r},t)$ is the electric charge density. ($\boldsymbol{\nabla} \cdot$) and ($\boldsymbol{\nabla} \times$) are the divergence and the curl operations, respectively.

Assume that the medium is linear, nondispersive, nonmagnetic, isotropic, and source free, i.e., no electric charges or currents ($\rho = 0, \boldsymbol{J} = 0$). Then, the relation between the electric flux density and the electric field becomes [8, 10, 11],

$$\boldsymbol{D}(\boldsymbol{r},t) = \epsilon(\boldsymbol{r})\, \boldsymbol{E}(\boldsymbol{r},t) \tag{2.5}$$

where, ϵ is the dielectric permittivity of the medium. It is assumed to vary slowly with position (nearly constant within a distance of a wavelength).

And, the relation between the magnetic flux density and the magnetic field becomes [8, 10, 11],

$$\boldsymbol{B}(\boldsymbol{r},t) = \mu_0\, \boldsymbol{H}(\boldsymbol{r},t) \tag{2.6}$$

where, μ_0 is the magnetic permeability of free space.

Accordingly, Maxwell's equations becomes,

$$\boldsymbol{\nabla} \times \boldsymbol{H}(\boldsymbol{r},t) - \epsilon(\boldsymbol{r})\, \frac{\partial \boldsymbol{E}(\boldsymbol{r},t)}{\partial t} = 0 \tag{2.7}$$

$$\boldsymbol{\nabla} \times \boldsymbol{E}(\boldsymbol{r},t) + \mu_0\, \frac{\partial \boldsymbol{H}(\boldsymbol{r},t)}{\partial t} = 0 \tag{2.8}$$

$$\boldsymbol{\nabla} \cdot \boldsymbol{E}(\boldsymbol{r},t) = 0 \tag{2.9}$$

$$\boldsymbol{\nabla} \cdot \boldsymbol{H}(\boldsymbol{r},t) = 0 \tag{2.10}$$

The Cartesian components of the electric field (E_x, E_y, E_z) and magnetic field (H_x, H_y, H_z) satisfies the scaler wave equation [8],

$$\boldsymbol{\nabla^2} u(\boldsymbol{r},t) - \frac{n^2(\boldsymbol{r})}{c_0^2} \frac{\partial^2 u(\boldsymbol{r},t)}{\partial t} = 0 \tag{2.11}$$

such that, u represents any of the six components of the electric and magnetic fields, $c_0 \approx 3 \times 10^8\ m/s$, is the speed of light in free space, $n = \sqrt{\epsilon/\epsilon_0}$ is the refractive index of the medium, ϵ_0 is the electric permittivity of free space, and $\boldsymbol{\nabla^2}$ is the Laplacian operator.

Tissue is an inhomogeneous medium, whose refractive index is continuously changing with position. It could be considered as a random medium whose refractive index changes randomly with position [12],

$$n(\boldsymbol{r}) = \bar{n} + \Delta(\boldsymbol{r}) \tag{2.12}$$

such that, $\bar{n}$ is the mean of the refractive index, and $\Delta(\boldsymbol{r})$ (the variation in the refractive index) is a random process.

Assume that the light incident on the tissue is monochromatic with angular frequency, ω. Then, Eq. (2.11), becomes time-independent, [2, 8, 10]:

$$\boldsymbol{\nabla^2} u(\boldsymbol{r}) + k_0^2\, n^2(\boldsymbol{r})\, u(\boldsymbol{r}) = 0 \tag{2.13}$$

such that, $k_0 = \omega/c_0$ is the wave number.

Eq. (2.13) could be written as,

$$(\boldsymbol{\nabla}^2 + k^2) u(\boldsymbol{r}) = -F(\boldsymbol{r})\, u(\boldsymbol{r}) \tag{2.14}$$

where, $F(\boldsymbol{r})$ is known as the scattering potential of the medium, equal,

$$F(\boldsymbol{r}) = k_0^2[n^2(\boldsymbol{r}) - 1] \tag{2.15}$$

Write $u(\boldsymbol{r})$ as the sum of the incident field $u^{(inc)}(\boldsymbol{r})$ and the scattered field $u(\boldsymbol{r})$,

$$u(\boldsymbol{r}) = u^{(inc)}(\boldsymbol{r}) + u^{(sc)}(\boldsymbol{r}) \tag{2.16}$$

Assume that, the incident field, $u^{(inc)}(\boldsymbol{r})$, is a plane wave (the usual case), then it satisfies the Helmholtz equation,

$$(\boldsymbol{\nabla}^2 + k^2)\, u^{(inc)}(\boldsymbol{r}) = 0 \tag{2.17}$$

Therefore, Eq. (2.14) is reduced to,

$$(\boldsymbol{\nabla}^2 + k^2)\, u^{(sc)}(\boldsymbol{r}) = -F(\boldsymbol{r})\, u(\boldsymbol{r}) \tag{2.18}$$

The solution of Eq. (2.18) can be written in terms of the Green's function $G(\boldsymbol{r}, \boldsymbol{r}')$ [9, 10],

$$u^{(sc)}(\boldsymbol{r}) = \int_V F(\boldsymbol{r}')u(\boldsymbol{r}')G(\boldsymbol{r}, \boldsymbol{r}')d^3\boldsymbol{r}' \tag{2.19}$$

Finally, by substituting the scattered field in Eq. (2.16) we reach,

$$u(\boldsymbol{r}) = u^{(inc)}(\boldsymbol{r}) + \int_V F(\boldsymbol{r}')u(\boldsymbol{r}')G(\boldsymbol{r},\boldsymbol{r}')d^3\boldsymbol{r}' \tag{2.20}$$

which is commonly known as the integral equation of potential scattering [9, 10].

2.2 Radiative transfer approach for light propagation

After a long debate about the nature of light, it has been proven that light could be treated as both a particle and a wave [2]. Light is made up of a large number of photon particles, where the energy of a photon is proportional to the light frequency. Statistically photons behave in a wave-like manner, and for a large number of photons, they can be treated as a wave [2].

In the RT approach, we focus on the energy of the EM wave (equivalent to the number of photons) rather than the electric and magnetic fields. The propagation of energy in a scattering medium has been modeled using the Radiative Transfer Equation (RTE) for over 100 years [9, 13]. The RTE can be derived from Maxwell's equations using the Poynting theorem for energy conservation [9]. To give insight about each term in the RTE, we will highlight how each term of the RTE is developed from the Poynting theorem, the detailed derivation can be found in [9].

2.2.1 Radiative Transfer Equation

Below it is assumed that the medium is linear, isotropic and locally homogeneous (the medium dielectric constant, ϵ, and magnetic permeability, μ, are nearly constant within the distance of a wavelength). Also, it is assumed that, the field is time harmonic, the electric and magnetic fields are mutually orthogonal.

The flow of the power of the EM wave is given by the Poynting vector $\boldsymbol{S}$, defined as [8, 9]

$$\boldsymbol{S} = \boldsymbol{E} \times \boldsymbol{H}^{*} \tag{2.21}$$

The Poynting vector is measured power per unit area. By writing the fields in terms of their magnitudes and direction unit vectors, $\boldsymbol{E} = |\boldsymbol{E}|\,\hat{\boldsymbol{e}}$ and $\boldsymbol{H} = |\boldsymbol{H}|\,\hat{\boldsymbol{h}}$, the direction of the Poynting vector (direction of energy propagation) is given by the unitary vector $\hat{\boldsymbol{s}} = \hat{\boldsymbol{e}} \times \hat{\boldsymbol{h}}$. Then the Poynting vector is written as $\boldsymbol{S} = |\boldsymbol{E}||\boldsymbol{H}|\,\hat{\boldsymbol{s}}$.

Light propagates at frequencies higher than the frequencies measured by conventional detectors [2, 9]. Therefore, detectors measure the time-averaged Poynting vector $\langle \boldsymbol{S}(\boldsymbol{r}) \rangle$.

The time-averaged conservation of energy at an arbitrary point $\boldsymbol{r}$, is given by the time-average of the Poynting's theorem [9],

$$\frac{1}{c}\frac{\partial \langle \boldsymbol{S}(\boldsymbol{r}) \rangle \cdot \hat{\boldsymbol{s}}}{\partial t} + \langle \frac{dP_{abs}(\boldsymbol{r})}{dV} \rangle + \boldsymbol{\nabla} \cdot \langle \boldsymbol{S}(\boldsymbol{r}) \rangle = 0 \tag{2.22}$$

where, $\frac{dP_{abs}}{dV} = \boldsymbol{J} \cdot \boldsymbol{E}$, is the absorbed power per unit volume.

Since the conservation of energy applies to any direction, then, from Eq. (2.22) the energy conservation for an arbitrary direction $\hat{\boldsymbol{v}}$, is given by [9],

$$\frac{1}{c}\frac{\partial \langle \boldsymbol{S}(\boldsymbol{r}) \rangle \cdot \hat{\boldsymbol{v}}}{\partial t} + \left\langle \frac{dP_{abs}(\boldsymbol{r})}{dV} \right\rangle (\hat{\boldsymbol{s}} \cdot \hat{\boldsymbol{v}}) + \hat{\boldsymbol{v}} \cdot \boldsymbol{\nabla}(\langle \boldsymbol{S}(\boldsymbol{r}) \rangle \cdot \hat{\boldsymbol{v}}) = 0 \tag{2.23}$$

To reach the RTE, we start by defining some important quantities,

1. The specific intensity, $I(\boldsymbol{r}, \hat{\boldsymbol{v}})$, is the power per unit area per unit solid angle flowing at $\boldsymbol{r}$ in direction $\hat{\boldsymbol{v}}$. It is given by the volume-average (over a small differential volume δV) of the time-averaged Poynting vector projected on direction $\hat{\boldsymbol{v}}$,

$$I(\boldsymbol{r}, \hat{\boldsymbol{v}}) = \frac{1}{4\pi\ \delta V} \int_{\delta V} \langle \boldsymbol{S}(\boldsymbol{r} - \boldsymbol{r}') \rangle \cdot \hat{\boldsymbol{v}}\ d^3\boldsymbol{r}' \tag{2.24}$$

2. The scattering phase function $p(\hat{\boldsymbol{v}}', \hat{\boldsymbol{v}})$, is the portion of energy that changes its propagation direction from $\hat{\boldsymbol{v}}'$ to $\hat{\boldsymbol{v}}$ [9]. It could be interpreted statistically as the probability of propagating in direction $\hat{\boldsymbol{v}}$ due to scattering of light propagating in direction $\hat{\boldsymbol{v}}'$[2, 12, 14]. The scattering phase function depends on the scattering behaviour of the medium [9]. In biomedical optics it is usually approximated by the Henyey-Greenstein's phase function. The Henyey-Greenstein's phase function describes the scattering behaviour of the medium in terms of the anisotropy factor, $g = \langle \hat{\boldsymbol{v}}' \cdot \hat{\boldsymbol{v}} \rangle$, equal to the mean of cosine the angle suspended between the incidence and scattering directions [9, 14].

Then, by averaging Eq. (2.23) over a small differential volume,

- The first term yields the temporal change of the specific intensity,

$$\frac{1}{c}\frac{\partial}{\partial t} I(\boldsymbol{r}, \hat{\boldsymbol{v}}) \tag{2.25}$$

- The second term is the origin of losses due to absorption, it becomes,

$$\mu_a\ I(\boldsymbol{r}, \hat{\boldsymbol{v}}) \tag{2.26}$$

  such that μ_a is the absorption coefficient.

- The time-averaged Poynting vector, $\langle \boldsymbol{S}(\boldsymbol{r}) \rangle$, could be written as the sum of two contributions $\langle \boldsymbol{S}^{(inc)}(\boldsymbol{r}) \rangle$, $\langle \boldsymbol{S}^{(sc)}(\boldsymbol{r}) \rangle$, the contributions from non-scattered light and scattered light respectively. The third term in Eq. (2.23) results in three components.

The first component is due to $\langle \boldsymbol{S}^{(inc)}(\boldsymbol{r})\rangle$, while the second and third components are due to $\langle \boldsymbol{S}^{(sc)}(\boldsymbol{r})\rangle$.

1- Spatial change in the specific intensity,

$$\hat{\boldsymbol{v}} \cdot \boldsymbol{\nabla} I(\boldsymbol{r}, \hat{\boldsymbol{v}}) \tag{2.27}$$

2- Energy lost due to scattering (energy scattered outside δV)

$$\mu_s \, I(\boldsymbol{r}, \hat{\boldsymbol{v}}) \tag{2.28}$$

such that μ_s is the scattering coefficient.

3- Energy gained due to the scattered light coming from adjacent differential volumes (energy scattered inside δV)

$$-\mu_s \int_{4\pi} I(\boldsymbol{r}, \hat{\boldsymbol{v}}') \, p(\hat{\boldsymbol{v}}', \hat{\boldsymbol{v}}) \, d\hat{\boldsymbol{v}}' \tag{2.29}$$

such that $d\hat{\boldsymbol{v}}'$ is the differential solid angle. Note that the factor μ_s in the above term comes from the definition used for the phase function [9, 14].

Finally, by accounting for a source term, $\epsilon(\boldsymbol{r}, \hat{\boldsymbol{v}})$, we reach the RTE in its familiar integro-differential form [9, 14],

$$\frac{1}{c}\frac{\partial}{\partial t} I(\boldsymbol{r}, \hat{\boldsymbol{v}}) + \hat{\boldsymbol{v}} \cdot \boldsymbol{\nabla} I(\boldsymbol{r}, \hat{\boldsymbol{v}}) + \mu_t \, I(\boldsymbol{r}, \hat{\boldsymbol{v}}) - \mu_s \int_{4\pi} I(\boldsymbol{r}, \hat{\boldsymbol{v}}') \, p(\hat{\boldsymbol{v}}', \hat{\boldsymbol{v}}) \, d\hat{\boldsymbol{v}}' = \epsilon(\boldsymbol{r}, \hat{\boldsymbol{v}}) \tag{2.30}$$

such that μ_t is the total extinction coefficient equal to the sum of μ_a and μ_s.

The first term in Eq. (2.30) could be neglected, due to the high speed of light (1/c factor), resulting in the steady-state equation [12, 15].

2.2.2 Specular reflection and refraction

The RTE assumes that the medium is homogeneous with constant refractive index, n. To model the flow of energy in inhomogeneous media using the RT approach, we have to handle the interaction of light at the interface between regions of different refractive indexes separately [9].

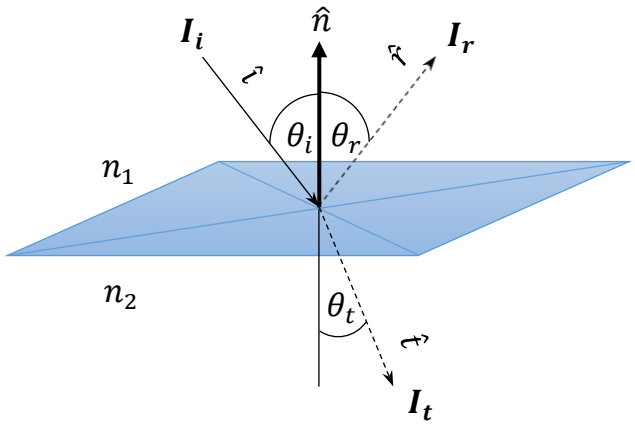

Figure 2.1 Reflection and transmittance at the surface between two different media

When a light beam meets a surface between two media of different refractive indices, it is either totally reflected or partially reflected and refracted (the two cases will be distinguished below). In partial reflection and refraction, the light beam splits into two beams one reflected back to the first medium, and the other is refracted and transmitted to the second medium. Fig. (2.1) shows a beam $\boldsymbol{I}_i$ (propagating in a region of refractive index n_1) incident on the surface of another region (refractive index n_2). The reflected beam, $\boldsymbol{I}_r$, the transmitted (refracted) beam, $\boldsymbol{I}_t$, the angles between the beams and the surface normal, $\hat{n}$, are shown in Fig. (2.1). The relation between the reflection angle θ_r and the incidence angle θ_i is given by the law of reflection,

$$\theta_r = \theta_i \tag{2.31}$$

The transmittance angle θ_t could be calculated using Snell's law [10, 14],

$$n_1 \sin(\theta_i) = n_2 \sin(\theta_t) \tag{2.32}$$

If $n_1 > n_2$ and θ_i is greater than the critical angle, $\theta_c = \sin^{-1}(n_2/n_1)$, then the light is totally reflected [10, 14]. This means that all the incident power is reflected, $|\boldsymbol{I}_i| = |\boldsymbol{I}_r|$, and no power is transmitted, $|\boldsymbol{I}_t| = 0$. Otherwise, light is partially reflected and refracted. The ratio between the power of the reflected and incident beams, known as the reflection coefficient, R, is given by Fresnel's formula,

$$R = \frac{|\boldsymbol{I}_r|}{|\boldsymbol{I}_i|} = \frac{1}{2}\left(\frac{\sin^2(\theta_i - \theta_t)}{\sin^2(\theta_i + \theta_t)} + \frac{\tan^2(\theta_i - \theta_t)}{\tan^2(\theta_i + \theta_t)}\right) \tag{2.33}$$

assuming that the light is *unpolarized* [9, 10, 14].

Accordingly, the transmittance, T, the ratio between the power of the transmitted and incident beams, is given by

$$T = \frac{|\boldsymbol{I}_r|}{|\boldsymbol{I}_i|} = 1 - R \tag{2.34}$$

Chapter 3

Optical Coherence Tomography theory and simulation

Optical Coherence Tomography (OCT) is a high-resolution optical imaging technique that creates subsurface cross-sectional images. OCT theory is analogous to ultrasonic pulse-echo imaging theory, except that OCT uses light waves rather than ultrasonic waves [1, 16]. OCT imaging resolution is few micrometers (1-15 μm), which is 10 - 100 times more than the imaging resolution of conventional ultrasound. However, OCT imaging penetration depth is limited to few millimeters (2-3 mm) from the tissue surface, which is much less than ultrasound imaging penetration depth [16]. OCT has many applications in the biomedical field and in other fields.

In ultrasonic pulse-echo imaging, pulses of ultrasonic waves are incident on tissue surface, the waves are reflected from internal structures and their echoes are measured. The position where the wave was reflected is calculated from the time delay between sending and receiving; then the image is constructed from the intensity of the echoes [16]. This methodology is not practical for light because light is approximately 1 million times faster than sound, i.e., we need ultrafast (femtosecond) pulses and detectors [16]. In OCT systems, the back-reflected light is combined with a reference light and their interference is measured [2, 16, 17]. Based on the interference profile tomographic images are constructed.

OCT imaging systems could be classified as time domain OCT (TDOCT), and frequency domain OCT (FDOCT) [2, 16]. Both of them relies on interferometry, but they differ in their design. In this thesis, we will focus on time domain OCT and its simulation.

3.1 Theory of time domain Optical Coherence Tomography

Time domain OCT theory is based on low coherence interferometry. The coherence of light is the degree of correlation between the optical field at different locations and time [2, 12, 16]. The coherence length of an optical source is the length over which two waves from a light source are coherent; it depends on the bandwidth of the source spectrum. Low coherence interferometry uses a broad-bandwidth light source to measure the time delay by comparing the reflected light with a reference light [2, 16, 17]. Maximum interference occurs when the optical path lengths of the reflected and reference light are precisely equal [2, 16, 17].

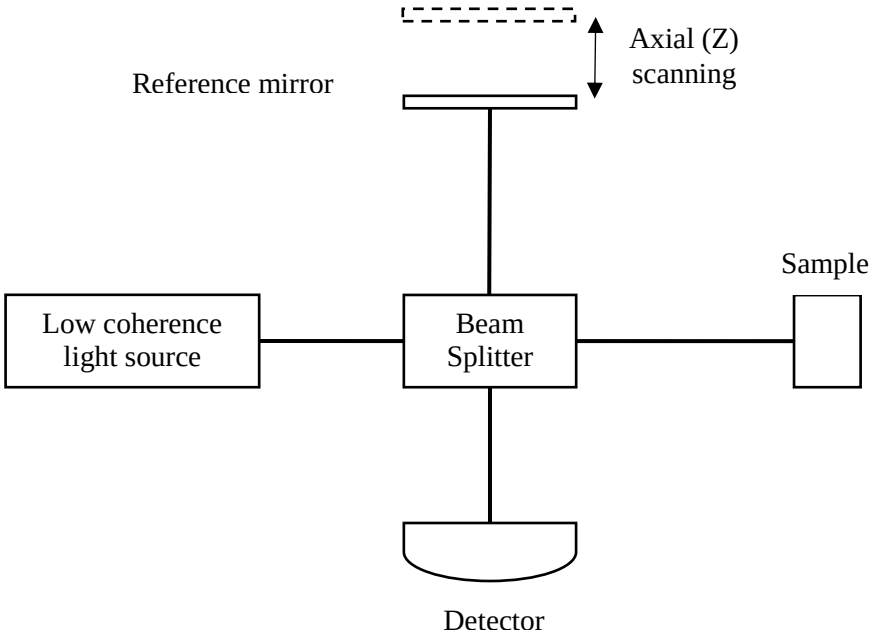

Figure 3.1. Time Domain OCT system schematic diagram

A simplified setup of a TDOCT system (Michelson type interferometer) is shown in Fig. (3.1) [2, 16, 17]. In TDOCT, light from a low coherence optical source is split (using a beam splitter) into two beams, a reference beam, and a sample beam. The reference beam is reflected back from a moving reference mirror. The sample beam is incident on the tissue sample and reflected back from different depths in the sample. The two reflected beams are combined and their interference is measured by a photodetector. Interference occurs between the reference beam and light reflected from the sample that has matching optical path length within the coherence length of the source. By moving the reference mirror, we change the optical path length of the reference beam, allowing interference with light coming from different depths in the sample. Accordingly, the OCT A-scan is obtained from the magnitude of the interference at different depth.

3.2 Monte Carlo simulation of TDOCT

To simulate the OCT signals from tissue, we need to model the propagation of light in scattering media. In 1983, Wilson and Adam introduced a Monte Carlo (MC) model, based on the RT approach, for light simulation in turbid media [18]. Since then their model has become popular, due to its accuracy and simplicity. It has been used to simulate light in homogeneous, multilayered [19, 20], and arbitrarily shaped scattering media [21-25].

The first OCT simulator was introduced in 1998 by Smithies *et al*. [26]. That simulator only considers homogeneous turbid media, i.e., the optical properties of the medium are the same all over its volume. In 1999, Yao and Wang developed a simulator for OCT signals from multilayered turbid media, i.e., media with parallel boundaries between regions of different optical properties [27]. Lima *et al*. then improved this simulator by

applying an advanced importance sampling technique, which reduced the simulation computation time by two orders of magnitude [28, 29]. In 2007, Kirillin *et al*. used sinusoidal functions to model the boundaries between regions with different optical properties and to simulate the OCT signals from such media [30]. Periyasamy and Pramanik developed an OCT simulator for multilayered turbid media with embedded, spherical, cylindrical, ellipsoidal, or cuboidal objects [31]. Then, those authors accelerated the simulation by using importance sampling [32].

Malektaji *et al*. introduced a simulator of the OCT signals for turbid media constructed of arbitrarily shaped regions that have different optical properties [17, 33]. To allow the inclusion of any structure, with the desired accuracy, they used tetrahedron meshes to model the media. Besides improving accuracy, the use of tetrahedrons reduce the simulation computation cost, compared with other ways for modeling arbitrarily shaped regions, such as triangular surface-meshes [17, 33]. They used an advanced importance sampling scheme that reduced the computational cost, but the simulation was still computationally expensive [17, 33]. Later in 2017, Escobar implemented the simulator introduced by Malektaji *et al.* on Graphics Processing Units (GPUs) using a Compute Unified Device Architecture (CUDA) platform by NVIDIA [34, 35]. The GPUs-based simulator, referred to by the name OCT Massively parallel simulator (OCT-MPS), was faster than the CPU-based simulator by more than one order of magnitude, which made OCT simulations with that method more practical [34, 35]. In the next section, we will review the main components of OCT-MPS, which we will use to build our simulator, and in the following section, we will highlight its limitation.

3.2.1 OCT Massively Parallel Simulator (OCT-MPS)

In OCT-MPS the medium is constituted of arbitrarily shaped regions of different optical properties. Each region is defined by the following parameters: scattering coefficient μ_s, absorption coefficient μ_a, refractive index n, and anisotropy factor g. A tetrahedron mesh is used to define the shape of the medium, identifying regions of different optical properties.

A large number of photon packets (a group of photons) are launched from an optical source and propagated in the medium while recording different quantities of interest. The tracing of the photon packets is performed simultaneously on the GPU threads. Each thread is responsible for the complete tracing of a photon packet. After a thread completes tracing a photon packet, it could start tracing a new packet if there are remaining packets not traced yet. Finally, the OCT signals are estimated from the expected value of the recorded quantities. Fig. (3.2) shows the flow chart of the photon propagation procedure used in OCT-MPS [35].

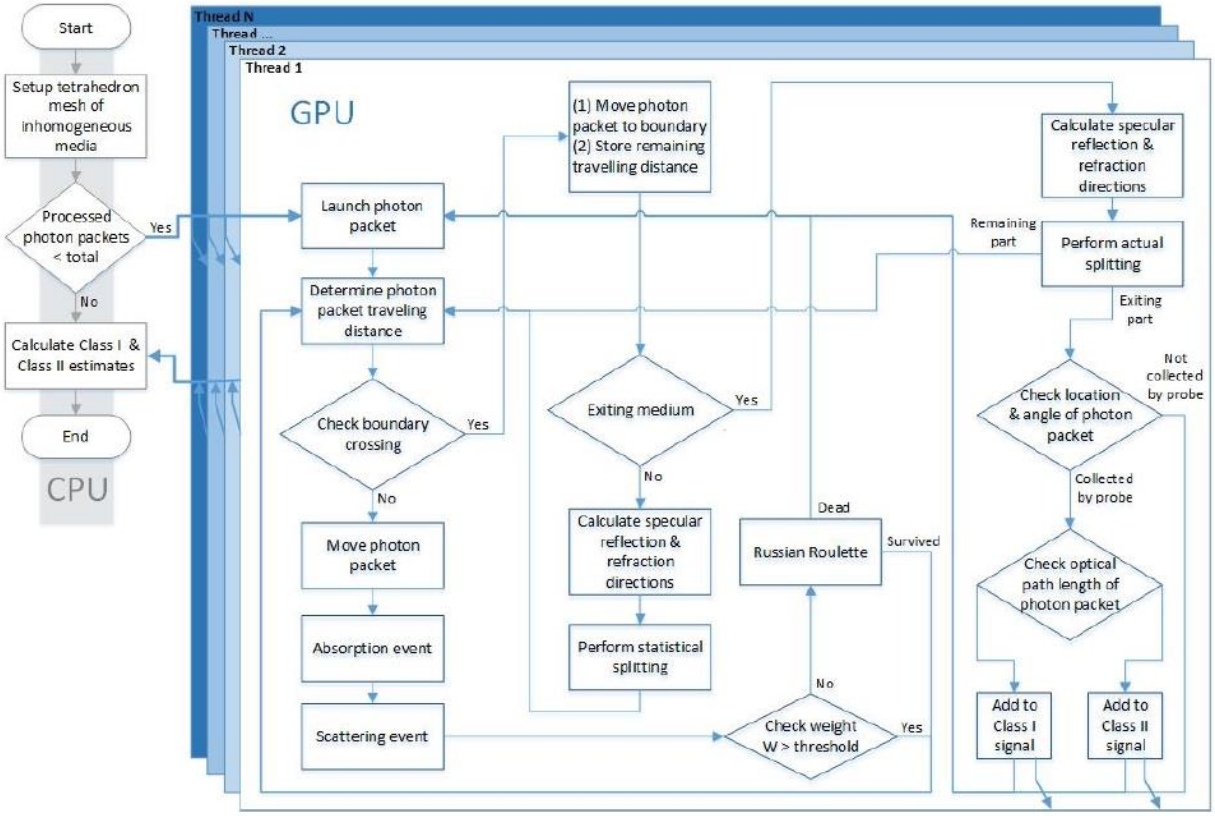

Figure 3.2. Flow chart of the photon propagation procedure in OCT-MPS (from Mauricio R. Escobar, M.Sc. thesis, 2015, p. 71)

3.2.1.1 Launching a Photon Packet

The light source is assumed to be an infinitely-thin incident beam (delta source). To speed up the simulation, photons are grouped in packets, rather than simulating one photon at a time. The weight of the photon packet represents the portion of the non-absorbed photons in the packet. The initial position and propagation direction for all the photon packets is the same, equal to the position and direction of emission of the source respectively. Their initial weight is set to unity, $W = 1$, i.e., non of the photons in the photon packet are absorbed.

3.2.1.2 Propagation in the medium

The packets are propagated inside the medium according to MC light simulation procedure for inhomogeneous media, as described in [21]. Photons undergo scattering and absorption at the so-called interaction sites. The distance between the interaction sites l, free path length, is a random variable. The cumulative distribution function (CDF) of l, is given by,

$$F_l(l) = 1 - e^{-\mu_t l} \tag{3.1}$$

where, μ_t is the total extinction coefficient, equal to the sum of μ_s and μ_a, of the region where the photon packet is traveling.

Let the photon packet position be $\boldsymbol{r}_{\mathrm{p}}$, its propagation direction be $\hat{\boldsymbol{v}}_{\mathrm{p}}$, and l_{p} be the randomly sampled free path length. The code checks whether the photon packet will remain in the same tetrahedron or move to another one. Let d be the distance from $\boldsymbol{r}_{\mathrm{p}}$ to the position on the tetrahedron face (of the enclosing tetrahedron) where the photon packet may intersect while propagating. If $l_{\mathrm{p}} < d$, i.e., the interaction site is in the same tetrahedron, the packet is moved to the interaction site, $\boldsymbol{r}_{\mathrm{p}} = \boldsymbol{r}_{\mathrm{p}} + l_{\mathrm{p}}\, \hat{\boldsymbol{v}}_{\mathrm{p}}$, to undergo scattering and absorption. Otherwise, the packet is moved to the intersection position on the tetrahedron face, $\boldsymbol{r}_{\mathrm{p}} = \boldsymbol{r}_{\mathrm{p}} + d\, \hat{\boldsymbol{v}}_{\mathrm{p}}$, and the un-walked distance is stored to be propagated in the new tetrahedron. The un-walked part of the sampled step is stored as,

$$s_{left} = (l_{\mathrm{p}} - d) \times \mu_t \tag{3.2}$$

where, s_{left} is dimensionless.

If the region of the new tetrahedron is different, specular reflection and refraction occur at the tetrahedron face (as explained in section 2.2.2). OCT-MPS is designed to trace one

photon packet at a time. Therefore, statistical splitting is preferred over actual splitting. In case that the transmitted photon packet will exit the medium, i.e., will no longer be traced, actual splitting is used. Otherwise, statistical splitting is used. In statistical splitting, the calculated Fresnel's coefficient of reflection, R, (a formula equivalent to Eq. (2.30) is used for computational efficiency) gives the probability of the reflection of the photon packet, accordingly the probability of transmission is $1 - R$.

Then, the un-walked part of the sampled step is similarly propagated in the new tetrahedron. The remaining part of the free path length is equal to,

$$l_{left} = \frac{s_{left}}{\mu_t} \tag{3.3}$$

such that, μ_t is the total extinction coefficient of the region of the enclosing tetrahedron (the new tetrahedron).

3.2.1.3 Scattering and Absorption

At the interaction sites, the photon packet undergoes scattering and absorption. A portion of the photons in the packet is absorbed, equal to,

$$\Delta W = W \times \frac{\mu_a}{\mu_t} \tag{3.4}$$

where, μ_a and μ_t are the absorption and total extinction coefficients, respectively, of the enclosing tetrahedron. Therefore, the weight of the packet after absorption is given by, $W = W - \Delta W$.

The photon packet scatters at the interaction site and changes its propagation direction based on the phase function. The Henyey-Greenstein phase function is the most commonly

used phase function in biomedical optics [9, 14]. The Henyey-Greenstein phase function is a probability density function, given by,

$$p^{(\mathrm{HG})}\left(\hat{\boldsymbol{v}}_{\mathrm{p}} \cdot \hat{\boldsymbol{v}}_{\mathrm{p}}{}'\right) = p^{(\mathrm{HG})}(\cos(\theta_s)) = \frac{1 - g^2}{2(1 + g^2 - 2g\cos(\theta_s))^{3/2}} \tag{3.5}$$

such that, $\hat{\boldsymbol{v}}_{\mathrm{p}}$, $\hat{\boldsymbol{v}}_{\mathrm{p}}{}'$, are the directions of propagation before and after scattering, θ_s is the angle between the two directions, i.e., $\cos(\theta_s) = \hat{\boldsymbol{v}}_{\mathrm{p}} \cdot \hat{\boldsymbol{v}}_{\mathrm{p}}{}'$, and g is the anisotropy factor of the phase function (depends on the medium). The azimuthal angle, φ_s, is a uniform random variable over the interval $[0, 2\pi]$.

The anisotropy factor of tissue is high. Therefore, the probability of backward scattering towards the OCT fiber probe is small. Importance sampling could be used to increase the probability of these rare events by biasing the propagation direction to the desired direction (towards the OCT fiber probe position) while recording the likelihood of the biased event. The likelihood of the biased event is used as a compensating function to obtain unbiased estimates of the OCT signals. The importance sampling scheme used in OCT-MPS is described in [29].

3.2.1.4 Random number generation

In OCT-MPS random numbers are generated using the CDF inversion method. This method relies on the one-to-one mapping between any two CDFs (any CDF is monotonically increasing from zero to one) [15, 36].

Let the random variable we want to sample be, x, and its CDF be, $F_x(x)$. Let u be a uniform random variable over the interval $[0, 1]$ (we could sample using pseudo-random number

generators). The inverse CDF method could be used to obtain samples of x from the samples of u,

$$x = F_x^{-1}(u) \tag{3.6}$$

When generating uniform random numbers (samples of u) in a parallel environment, we want to avoid any inter-thread and intra-thread correlations. OCT-MPS uses an improved implementation of the Multiply-With-Carry method to generate uniform random numbers in its parallel environment [37, 38]. OCT-MPS has three independent streams of random numbers, one is used for the scattering function (scattering direction), the other is used for reflection and refraction function, and the third is used for random number generation in the remaining functions. The seed of each stream could either be set manually (different seed for each stream) or obtained from the system's clock. The seed of each thread is a unique safe prime number (a prime number that has the form, 2 p + 1, where p is also a prime number) [34, 35].

3.2.1.5 Photon tracing termination

The tracing of a photon packet ends when it is collected by the OCT fiber probe or exits the medium. While propagating in the medium, the photon packet weight decreases due to absorption. After the photon packet weight decrease below a certain threshold (the threshold used is 10^{-4}), the tracing of the packet is terminated with probability $1 - \frac{1}{m}$. If the packet survives (probability of survival is $\frac{1}{m}$), its weight will be multiplied by the factor m (m is set to 10 in the simulator). This method is known by *Russian Roulette*, it is an unbiased technique that speeds up the simulation.

3.2.1.6 Estimation of Class I and Class II diffuse reflectance

In OCT-MPS the fiber probe, of diameter Φ_{f} and acceptance angle θ_{f}, is placed in direct contact with the surface of the medium (tissue). The surface of the medium is in the XY-plane, i.e., $z = 0$, and normal to the z-axis. The packets are collected by the fiber if they hit its surface with an angle that does not exceed the acceptance angle (θ_{f}). Information about the collected photon packets is used to estimate the OCT signals (Class I and Class II diffuse reflectance). Class I diffuse reflectivity is due to photons scattered within the coherence length of the optical source. While Class II diffuse reflectivity is due to photons multiply scattered beyond the source coherence length. Class I photon packets, reflected from a depth z, are identified by the spatial-temporal indicator function below,

$$\mathbb{1}_{\mathrm{I}}(z,i) := \begin{cases} 1 & l_c > \left|\Delta l^{(i)} - 2z_{\max}^{(i)}\right|, 2r^{(i)} < \Phi_{\mathrm{f}},\ \theta_z^{(i)} < \theta_{\mathrm{f}}, \left|\Delta l^{(i)} - 2z\right| < l_c \\ 0 & otherwise \end{cases} \quad (3.7)$$

such that, l_c is the coherence length of the optical source, z is the depth imaged, $\Delta l^{(i)}$ is the optical path length of the i^{th} packet, $z_{\max}^{(i)}$ is the maximum depth reached by the i^{th} packet, $r^{(i)}$ is the distance between the packet exit position and fiber probe centre position, and $\theta_z^{(i)}$is the angle between the packet propagation direction and the z-axis for the i^{th} packet. A similar function is used for identifying Class II photon packet,

$$\mathbb{1}_{\mathrm{II}}(z,i) := \begin{cases} 1 & l_c < \left|\Delta l^{(i)} - 2z_{\max}^{(i)}\right|, 2r^{(i)} < \Phi_{\mathrm{f}},\ \theta_z^{(i)} < \theta_{\mathrm{f}}, \left|\Delta l^{(i)} - 2z\right| < l_c \\ 0 & otherwise \end{cases} \quad (3.8)$$

Finally, Class I diffuse reflectance, $R_{\mathrm{I}}(z)$, and Class II diffuse reflectance, $R_{\mathrm{II}}(z)$, at a depth z, are estimated by,

$$\widehat{\mathrm{R}}_{\mathrm{I,II}}(z) = \frac{1}{N}\sum_{i=1}^{N} \mathbb{1}_{\mathrm{I,II}}(z,i)L(i)W(i) \tag{3.9}$$

where N is the total number of photon packets simulated, $L(i)$ is the likelihood value of the i^{th} packet, and $W(i)$ is the weight of the i^{th} packet. In addition, the error in the estimate $\widehat{\mathrm{R}}_{\mathrm{I,II}}$ is given by the estimate of its variance,

$$\hat{e}^2_{\mathrm{I,II}}(z) = \frac{1}{N(N-1)}\sum_{i=1}^{N}\left(\mathbb{1}_{\mathrm{I,II}}(z,i)L(i)W(i) - \widehat{\mathrm{R}}_{\mathrm{I,II}}(z)\right)^2 \tag{3.10}$$

3.2.2 Limitation of the Massively Parallel OCT (OCT-MPS) Simulator

In OCT-MPS, the OCT fiber probe is placed in direct contact with the medium. The light emitted from the OCT fiber is assumed to be an infinitely thin beam, i.e., the probing area is infinitely small, which is not a realistic assumption. Typically, the signal due to a finite incident beam could be approximated by repeating the simulation at a set of points over the incident beam area, then get the superposition of the results. But, this approach is computationally expensive, as it requires repeating the simulation at each point, this is referred to as the superposition-based simulation approach.

Chapter 4

Solution of Linear Integral Equations using Monte Carlo Methods

In many cases, the closed-form solution of an integral cannot be reached, especially when the dimension of the integral is high. Monte Carlo (MC) methods could be used as a quadrature method to estimate high dimensional integrals. Fredholm integral equations of the second kind commonly appear in a lot of problems, such as light scattering. Solving these equation requires solving an infinite summation of integrals with increasing dimensions. In this chapter, we will explain how MC methods could be used to solve integrals, focusing on the Fredholm integral equation of the second kind.

4.1 Solving high dimensional Integrals using Monte Carlo

To estimate an integral using Monte Carlo, it has to be written in the form of an expectation, i.e.,

$$I = \mathbf{E}_{p_x}\{g(x)\} = \int g(x)\, p_x(x)\, dx \tag{4.1}$$

where, $p_x(x)$ is a probability distribution.

The integral above could be estimated using Monte Carlo, by randomly sampling x, from the distribution $p_x(x)$. Then, the estimate is given by [15, 36],

$$\widehat{I_k} = \frac{1}{N}\sum_{i=1}^{N} g\left(X^{(i)}\right) \tag{4.2}$$

such that, $X^{(i)}$ are samples from $p_x(x)$, and N are the number of samples.

For a large N, the error in the estimate is given by, $|e_I| \cong \frac{\sigma_I}{\sqrt{N}}$, where [15, 36],

$$\sigma_I^2 \equiv \mathbf{var}_{p_g}\{g(x)\} = \int g^2(x)\, p_x(x)\, dx - I^2 \tag{4.3}$$

Consider a general k-dimensional integral, not given in the form of an expectation,

$$I_k = \int_{V_k} f_k(x_{1:k})\, dx_{1:k} \tag{4.4}$$

where, $x_{1:k} \equiv \{x_1, x_2 \ldots, x_k\}$ are the variables of the integral, $f_k(x_{1:k})$ is the integrand. To solve such integral using Monte Carlo, it must be written in the form of an expectation; this could be done using importance sampling [15, 36]. Importance sampling relies on proposing a probability distribution, $q_k(x_{1:k})$, that could be sampled, such that,

$$q_k(x_{1:k}) > 0 \quad \forall \; f_k(x_{1:k}) \neq 0 \tag{4.5}$$

Then, the integral in Eq. (4.4) could be written as an expectation under $q_k(x_{1:k})$,

$$I_k = \int_{V_k} f_k(x_{1:k}) dx_{1:k} = \int \frac{f_k(x_{1:k})}{q_k(x_{1:k})}\, q_k(x_{1:k})\, dx_{1:k} = \mathbf{E}_{q_k}\left\{\frac{f_k(x_{1:k})}{q_k(x_{1:k})}\right\} \tag{4.6}$$

Then, the MC estimate of I_k is given by,

$$\widehat{I_k} = \frac{1}{N}\sum_{i=1}^{N} \frac{f_k\left(X_{1:k}^{(i)}\right)}{q_k\left(X_{1:k}^{(i)}\right)} \tag{4.7}$$

where, $X_{1:k}^{(i)}$ are samples from $q_k(x_{1:k})$, and N are the number of samples.

And, the error in the estimate, $\left|e_{I_k}\right| \cong \frac{\sigma_{I_k}}{\sqrt{N}}$, where,

$$\sigma_{I_k}^2 \equiv \mathbf{var}_{q_k}\left\{\frac{f_k(x_{1:k})}{q_k(x_{1:k})}\right\} = \int \frac{f_k^2(x_{1:k})}{q_k^2(x_{1:k})}\, q_k(x_{1:k}) dx_{1:k} - I_k^2 \tag{4.8}$$

It is clear from the above equation that the error strongly depends on our choice of $q_k(x_{1:k})$.

4.1.1 Minimizing the variance

To minimize the error in the estimate, we need to find and sample the distribution, $q_k^*(x_{1:k})$, that minimizes the variance, $\sigma_{I_k}^2$, given in Eq. (4.8). It could be showed that, $q_k^*(x_{1:k})$ is equal to [36],

$$q_k^*(x_{1:k}) = \frac{|f_k(x_{1:k})|}{Z_{f_k}} \tag{4.9}$$

where, Z_{f_k} is the normalizing constant, equal to,

$$Z_{f_k} = \int_{V_k} |f_k(x_{1:k})| dx_{1:k} \tag{4.10}$$

Then, the estimate of the integral, I_k, becomes,

$$\widehat{I_k} = \frac{1}{N}\sum_{i=1}^{N} \frac{f_k(X_{1:k}^{(i)})}{q_k(X_{1:k}^{(i)})} = \frac{1}{N}\sum_{i=1}^{N} \frac{f_k(X_{1:k}^{(i)})}{|f_k(X_{1:k}^{(i)})|} Z_{f_k} \tag{4.11}$$

where, $X_{1:k}^{(i)}$ are samples from $q_k^*(x_{1:k})$, N are the number of samples.

If, $f_k(x_{1:k})$, is always positive, then, the normalizing constant, $Z_{f_k} = I_k$, the integral itself, Eq. (4.11) becomes,

$$\widehat{I_k} = \frac{1}{N}\sum_{i=1}^{N} \frac{f_k(X_{1:k}^{(i)})}{f_k(X_{1:k}^{(i)})} I_k = \frac{1}{N}\sum_{i=1}^{N} I_k \tag{4.12}$$

And, Eq. (4.8), the variance becomes equal to zero, i.e., one sample is enough to give the exact answer.

It is clear that to reach the minimum variance we need to evaluate Z_{f_k}, which is a high dimensional integral (equal to the integral we want to solve, I_k, when $f_k(x_{1:k})$ is always

positive). Even though, we cannot use $q_k^*(x_{1:k})$ in practice, this result tells us that using a distribution close to $q_k^*(x_{1:k})$ will reduce the variance [36].

4.2 Solution of the Fredholm Integral Equations of the second kind using Sequential Importance sampling.

Consider the Fredholm integral equation of the second kind below,

$$y(\boldsymbol{x}) = g(\boldsymbol{x}) + \int_V y(\boldsymbol{x}')\, B(\boldsymbol{x}', \boldsymbol{x})\, d\boldsymbol{x}', \quad \boldsymbol{x}' \epsilon V \tag{4.13}$$

This equation could be thought of as a system with $g(\boldsymbol{x})$ as input and $y(\boldsymbol{x})$ is output [39]. The presence of $y(\boldsymbol{x})$, the unknown output, inside the integral makes solving such equations difficult. To solve Eq. (4.13) we could write it in different integrative forms, one of them is [39-41],

$$y^{(k)}(\boldsymbol{x}) = g(\boldsymbol{x}) + \int y^{(k-1)}(\boldsymbol{x}')\, B(\boldsymbol{x}', \boldsymbol{x})\, d\boldsymbol{x}', \qquad y^{(0)}(\boldsymbol{x}) = g(\boldsymbol{x}) \tag{4.14}$$

where, $k = 0, 1, 2, \ldots \infty$, then $y(\boldsymbol{x})$ is approximated by a series known as the Neumann's series, equal to,

$$\begin{aligned} y(\boldsymbol{x}) = g(\boldsymbol{x}) &+ \int g(\boldsymbol{x}_0)\, B(\boldsymbol{x}_0, \boldsymbol{x})\, d\boldsymbol{x}_0 + \iint g(\boldsymbol{x}_0)\, B(\boldsymbol{x}_0, \boldsymbol{x_1}) B(\boldsymbol{x}_1, \boldsymbol{x})\, d\boldsymbol{x}_{0:1} \\ &+ \iiint g(\boldsymbol{x}_0)\, B(\boldsymbol{x}_0, \boldsymbol{x}_1) B(\boldsymbol{x}_1, \boldsymbol{x}_2) B(\boldsymbol{x}_2, \boldsymbol{x})\, d\boldsymbol{x}_{0:2} + \cdots \end{aligned} \tag{4.15}$$

A sufficient condition for the convergence of this series is that the spectral radius of the kernel $B(\boldsymbol{x}', \boldsymbol{x})$ should be less than one [15, 42]. Assuming that the series converges, then,

$$y(\boldsymbol{x}) = \lim_{k \to \infty} y^{(k)}(\boldsymbol{x}) \tag{4.16}$$

Each term in the series contributes to the output; the first term is the direct contribution of the input, the second term is the contribution of the input after applying the kernel once to it, and, the k^{th} term is the contribution of the input after applying the kernel $(k-1)$ times to it.

Monte Carlo could be used to get the inner product of $y(\boldsymbol{x})$ with a weighting function, $h(\boldsymbol{x})$, defined based on our interest [15, 36]. Let, the quantity of interest be Q, equal to

$$Q = \int y(\boldsymbol{x})h(\boldsymbol{x})d\boldsymbol{x} \cong \sum_{k=0}^{K}\left(\iint_{k+1} g(\boldsymbol{x}_0)\prod_{i=0}^{i=k} B(\boldsymbol{x}_{i-1},\boldsymbol{x}_i)\,h(\boldsymbol{x}_k)\,d\boldsymbol{x}_{0:k}\right) \tag{4.17}$$

Any integral in the series could be solved using an MC based quadrature as explained in the above section. Technically, the proposed distribution $q_k(\boldsymbol{X}_{1:k})$ could be any distribution satisfying the conditions in Eq. (4.5) However, the dependence between each two consecutive variables, proposes using a *sequential importance sampling* strategy.

4.2.1 Sequential Importance Sampling (SIS)

Sequential Importance Sampling (SIS) is a sampling strategy where the proposed distribution, $q_k(\boldsymbol{x}_{0:k})$, has the structure [43],

$$q_k(\boldsymbol{x}_{0:k}) = q_k(\boldsymbol{x}_k|\boldsymbol{x}_{k-1})\ldots\ q_1(\boldsymbol{x}_1|\boldsymbol{x}_0)\,q_0(\boldsymbol{x}_0) \tag{4.18}$$

The distribution, $q_k(\boldsymbol{x}_{0:k})$, is constructed such that, each random variable, $\boldsymbol{x}_i$, is conditionally independent of all the previous variables except the last one, namely, $q_i(\boldsymbol{x}_i|\boldsymbol{x}_{1:\,i-1}) = q_i(\boldsymbol{x}_i|\boldsymbol{x}_{i-1})$, for, $i = 1, \ldots k$ [39, 43].

For sampling $q_k(\boldsymbol{x}_{0:k})$, the equation above could be reordered to,

$$q_k(\boldsymbol{x}_{0:k}) =\ q_0(\boldsymbol{x}_0)\,q_1(\boldsymbol{x}_1|\boldsymbol{x}_0)\ \ldots\ q_k(\boldsymbol{x}_k|\boldsymbol{x}_{k-1}) \tag{4.19}$$

Meaning, to get a sample of the variables $\boldsymbol{x}_{0:k}$ from the distribution $q_k(\boldsymbol{x}_{0:k})$, we first sample, $\boldsymbol{x}_0 \sim q_0(\boldsymbol{x}_0)$, then $\boldsymbol{x}_1 \sim q_1(\boldsymbol{x}_1|\boldsymbol{x}_0)$, till $\boldsymbol{x}_k \sim q_k(\boldsymbol{x}_k|\boldsymbol{x}_{k-1})$. This is a relatively easy sampling approach because each component $(\boldsymbol{x}_1, \boldsymbol{x}_2, \dots, \boldsymbol{x}_k)$, is sampled from a low dimensional distribution.

By choosing, $q_0(\boldsymbol{x})$, such that,

$$q_0(\boldsymbol{x}) \neq 0 \quad \forall \quad g(\boldsymbol{x}) \neq 0 \tag{4.20}$$

And choosing, $q_i(\boldsymbol{x}_i|\boldsymbol{x}_{i\text{-}1}) = T(\boldsymbol{x}_i|\boldsymbol{x}_{i\text{-}1})$, where, $T(\boldsymbol{x}', \boldsymbol{x})$ is a probability transition kernel (which gives the probability of $\boldsymbol{x}$ given $\boldsymbol{x}'$), such that,

$$T(\boldsymbol{x}', \boldsymbol{x}) > 0, \qquad \text{for all} \qquad K(\boldsymbol{x}', \boldsymbol{x}) \neq 0 \tag{4.21}$$

Then, the proposed sequential importance sampling distribution, $q_k(\boldsymbol{x}_{0:k})$, would be equal to,

$$q_k(\boldsymbol{x}_{0:k}) = q_0(\boldsymbol{x}_0) \prod_{i=1}^{k} T(\boldsymbol{x}_i|\boldsymbol{x}_{i\text{-}1}) \tag{4.22}$$

satisfies the condition in Eq. (4.5)

And Eq. (4.17) could be altered and written as a series of expectations under the distributions $\{q_k(\boldsymbol{x}_{0:k})\}_{k=0:K}$.

$$Q \cong \sum_{k=0}^{K} \left(\mathbf{E}_{q_k} \left\{ \frac{g(\boldsymbol{x}_0)}{q_0(\boldsymbol{x}_0)} \prod_{i=0}^{i=k} \frac{K(\boldsymbol{x}_{i-1}, \boldsymbol{x}_i)}{T(\boldsymbol{x}_i|\boldsymbol{x}_{i\text{-}1})} h(\boldsymbol{x}_k) \right\} \right) \tag{4.23}$$

Finally, the above equation could be estimated using a large number, N, of samples from $\{q_k(\boldsymbol{x}_{0:k})\}_{k=0:K}$,

$$\hat{Q} = \frac{1}{N}\sum_{j=1}^{N}\sum_{k=0}^{K}\frac{g\left(\boldsymbol{X}_0^{(j)}\right)}{q_0\left(\boldsymbol{X}_0^{(j)}\right)}\prod_{i=0}^{i=k}\frac{K\left(\boldsymbol{X}_{i-1}^{(j)},\boldsymbol{X}_i^{(j)}\right)}{T\left(\boldsymbol{X}_i^{(j)}\middle|\boldsymbol{X}_{i\text{-}1}^{(j)}\right)}h\left(\boldsymbol{X}_k^{(j)}\right) \tag{4.24}$$

such that, $\boldsymbol{X}_i^{(j)}$ is the i^{th} component of the j^{th} sample chain.

We note that, when using this sampling approach, the chains are independent of the weighting function $h(\boldsymbol{x})$, therefore, we could use the chains to estimate several quantities of interest, i.e., inner products with different $h(\boldsymbol{x})$ weighting functions.

Chapter 5

Solution of Radiative Transfer Equation for homogeneous media

This chapter, will focus on applying the MC methods discussed in chapter 4 to solve the steady state RTE for homogeneous media. First, we will show how to write the steady-state RTE for homogeneous media in a linear integral form. Then, a solution using the MC methods discussed in the previous chapter, will be presented. Finally, the correspondence between the solution presented and the common MC simulation procedure for light propagation, will be established.

5.1 Linear Integral form of the RTE

Recall that the RTE in its integro-differential form,

$$\frac{1}{c}\frac{\partial}{\partial t} I(\boldsymbol{r},\hat{\boldsymbol{v}}) + \hat{\boldsymbol{v}}\cdot\boldsymbol{\nabla} I(\boldsymbol{r},\hat{\boldsymbol{v}}) + \mu_t\, I(\boldsymbol{r},\hat{\boldsymbol{v}}) = \epsilon(\boldsymbol{r},\hat{\boldsymbol{v}}) + \mu_s \int_{4\pi} I(\boldsymbol{r},\hat{\boldsymbol{v}}')\, p(\hat{\boldsymbol{v}}',\hat{\boldsymbol{v}})\, d\hat{\boldsymbol{v}}' \qquad (5.1)$$

Define, $\chi(\boldsymbol{r},\hat{\boldsymbol{v}})$, the particle emission density, to be equal to the right-hand side of Eq. (5.1),

$$\chi(\boldsymbol{r},\hat{\boldsymbol{v}}) = \epsilon(\boldsymbol{r},\hat{\boldsymbol{v}}) + \mu_s \int_{4\pi} I(\boldsymbol{r},\hat{\boldsymbol{v}}')\, p(\hat{\boldsymbol{v}}',\hat{\boldsymbol{v}})\, d\hat{\boldsymbol{v}}' \qquad (5.2)$$

The particle emission rate density, $\chi(\boldsymbol{r},\hat{\boldsymbol{v}})$, represents the amount of energy (per unit volume per unit time) emitted at $\boldsymbol{r}$ propagating in direction $\hat{\boldsymbol{v}}$, which is equal to the sum of,

1- The emission due to a source at $\boldsymbol{r}$ radiating in the direction $\hat{\boldsymbol{v}}$ (the term $\epsilon(\boldsymbol{r},\hat{\boldsymbol{v}})$).

2- The emissions due to light that scatters at $\boldsymbol{r}$ from an arbitrary direction, $\hat{\boldsymbol{v}}'$, to start propagating in $\hat{\boldsymbol{v}}$ direction.

According to the definition of the emission rate density in Eq. (5.2), Eq. (5.1) becomes,

$$\chi(\boldsymbol{r},\hat{\boldsymbol{v}}) = \hat{\boldsymbol{v}}\cdot\boldsymbol{\nabla} I(\boldsymbol{r},\hat{\boldsymbol{v}}) + \mu_t I(\boldsymbol{r},\hat{\boldsymbol{v}}) \tag{5.3}$$

The term, $\hat{\boldsymbol{v}}\cdot\boldsymbol{\nabla} I(\boldsymbol{r},\hat{\boldsymbol{v}})$, represents the spatial change of the specific intensity, it could be written as the rate of change of $I(\boldsymbol{r},\hat{\boldsymbol{v}})$ along the direction $-\hat{\boldsymbol{v}}$, as explained below.

Let, l be the distance between $\boldsymbol{r}$, and an arbitrary point $\boldsymbol{r}'$ along the direction $-\hat{\boldsymbol{v}}$, see Fig. (5.1), then, the direction $\hat{\boldsymbol{v}}$ could be written as,

$$\hat{\boldsymbol{v}} = \frac{\boldsymbol{r}-\boldsymbol{r}'}{l} \tag{5.4}$$

Let, dk, be a differential distance along the direction of the gradient, ∇I, then the magnitude of the gradient could be written as, $\frac{dI}{dk}$. And, let θ be the angle between the direction of the gradient and $\hat{\boldsymbol{v}}$ as shown in Fig. (5.1).

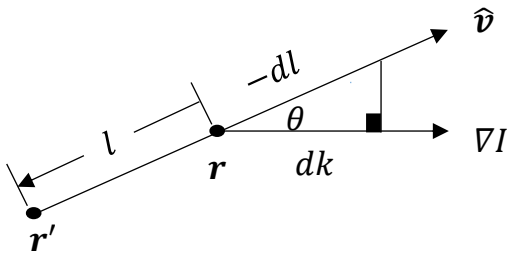

Figure 5.1. Representation of the inner product, $\hat{\boldsymbol{v}}\cdot\boldsymbol{\nabla} I(\boldsymbol{r},\hat{\boldsymbol{v}})$, as the rate of change of specific intensity along the direction $\hat{\boldsymbol{v}}$.

Therefore, from Fig. (5.1), the inner product, $\hat{\boldsymbol{v}}\cdot\boldsymbol{\nabla} I(\boldsymbol{r},\hat{\boldsymbol{v}})$, can be written as,

$$\hat{\boldsymbol{v}}\cdot\boldsymbol{\nabla} I(\boldsymbol{r},\hat{\boldsymbol{v}}) = \cos(\theta)\frac{dI(\boldsymbol{r},\hat{\boldsymbol{v}})}{dk} = \frac{dk}{-dl}\,\frac{dI(\boldsymbol{r},\hat{\boldsymbol{v}})}{dk} = -\frac{dI(\boldsymbol{r},\hat{\boldsymbol{v}})}{dl} \tag{5.5}$$

Accordingly, Eq. (5.1) becomes,

$$-\frac{dI(\boldsymbol{r},\hat{\boldsymbol{v}})}{dl} + \mu_t I(\boldsymbol{r},\hat{\boldsymbol{v}}) = \chi(\boldsymbol{r},\hat{\boldsymbol{v}}) \tag{5.6}$$

By multiplying both sides of Eq. (5.6) by $e^{-\mu_t l}$, the left-hand side becomes,

$$-e^{-\mu_t l}\,\frac{dI(\boldsymbol{r},\hat{\boldsymbol{v}})}{dl}+e^{-\mu_t l}\,\mu_t\,I(\boldsymbol{r},\hat{\boldsymbol{v}})=\frac{d}{dl}\{-I(\boldsymbol{r},\hat{\boldsymbol{v}})\,e^{-\mu_t l}\} \tag{5.7}$$

Then, Eq. (5.6) could be written as

$$\frac{d}{dl}\{-I(\boldsymbol{r},\hat{\boldsymbol{v}})\,e^{-\mu_t l}\}=\chi(\boldsymbol{r},\hat{\boldsymbol{v}})\,e^{-\mu_t l} \tag{5.8}$$

Assume that the medium is infinite, then by integrating Eq. (5.8), over l, the left-hand side is reduced to,

$$\int_{l=0}^{\infty}\frac{d}{dl}\{-I(\boldsymbol{r},\hat{\boldsymbol{v}})\,e^{-\mu_t l}\}\,dl=-I(\boldsymbol{r}_{\infty},\hat{\boldsymbol{v}})\,e^{-\mu_t\infty}+\,I(\boldsymbol{r},\hat{\boldsymbol{v}})=I(\boldsymbol{r},\hat{\boldsymbol{v}}) \tag{5.9}$$

Then, the specific intensity is given by,

$$I(\boldsymbol{r},\hat{\boldsymbol{v}})=\int_{l=0}^{\infty}\chi(\boldsymbol{r}-l\,\hat{\boldsymbol{v}},\hat{\boldsymbol{v}})\;e^{-\mu_t l}\;dl\equiv\int_{l=0}^{\infty}\chi(\boldsymbol{r}',\hat{\boldsymbol{v}})\;e^{-\mu_t l}\;dl \tag{5.10}$$

where, $\boldsymbol{r}'\equiv\boldsymbol{r}-l\,\hat{\boldsymbol{v}}$, is defined as a point along the direction $-\hat{\boldsymbol{v}}$ (see Fig. (5.2)).

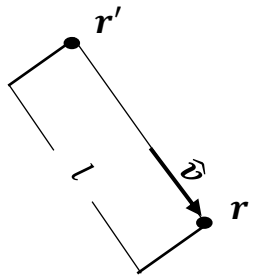

Figure 5.2 Specific Intensity arriving at $\boldsymbol{r}$ with direction $\hat{\boldsymbol{v}}$, it is due to all the emissions from any point, $\boldsymbol{r}'$, along the direction $-\hat{\boldsymbol{v}}$.

This result shows that the intensity arriving at the position $\boldsymbol{r}$ in direction $\hat{\boldsymbol{v}}$ is the result of the emissions from all other points along the direction $-\hat{\boldsymbol{v}}$ (see Fig. (5.2)).

Finally, by substituting Eq. (5.2) (the definition of the emission rate density) in Eq. (5.9) we reach the RTE in a linear integral form,

$$I(\boldsymbol{r},\hat{\boldsymbol{v}}) = \int_{l=0}^{\infty} \epsilon(\boldsymbol{r} - l\,\hat{\boldsymbol{v}},\hat{\boldsymbol{v}}) e^{-\mu_t l}\; dl$$
$$+ \mu_s \int_{l=0}^{\infty} \int_{4\pi} I(\boldsymbol{r} - l\,\hat{\boldsymbol{v}},\hat{\boldsymbol{v}}')\; p(\hat{\boldsymbol{v}}',\hat{\boldsymbol{v}}) e^{-\mu_t l}\; d\hat{\boldsymbol{v}}' dl \tag{5.10}$$

We could illustrate the above equation using Fig. (5.3), the intensity arriving at $\boldsymbol{r}$ in direction $\hat{\boldsymbol{v}}$, is due to light coming from,

- Sources along the direction $-\hat{\boldsymbol{v}}$.
- Scattering that occurs at any position along the direction $-\hat{\boldsymbol{v}}$, from any arbitrary direction $\hat{\boldsymbol{v}}'$ to the direction $\hat{\boldsymbol{v}}$.

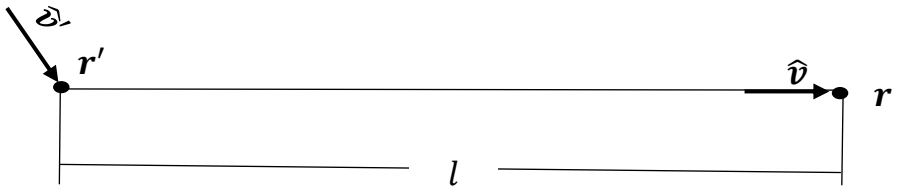

Figure 5.3. Intensity arriving at position $\boldsymbol{r}$ with propagation direction $\hat{\boldsymbol{v}}$ due to radiation scattering at a position along the direction $-\hat{\boldsymbol{v}}$.

Let, $\boldsymbol{p} \equiv (\boldsymbol{r},\hat{\boldsymbol{v}})$, be the radiation state, defined by the position $\boldsymbol{r}$ and direction of propagation $\hat{\boldsymbol{v}}$. Then, the above equation could be written in the compact form,

$$I(\boldsymbol{p}) = \tilde{\epsilon}(\boldsymbol{p}) + \iint I(\boldsymbol{p}')\, B(\boldsymbol{p}',\boldsymbol{p})\; dl\; d\hat{\boldsymbol{v}} \tag{5.11}$$

such that,

- $\boldsymbol{r}'$ is defined as a position away from $\boldsymbol{r}$ by a distance l along the direction $-\hat{\boldsymbol{v}}$,

$$\boldsymbol{r}' = \boldsymbol{r} - l\,\hat{\boldsymbol{v}} \tag{5.12}$$

- $\epsilon(\boldsymbol{p})$ is the source emission term, $\tilde{\epsilon}(\boldsymbol{p})$ is the source contribution to $I(\boldsymbol{p})$, equal to,

$$\tilde{\epsilon}(\boldsymbol{r}, \hat{\boldsymbol{v}}) = \int_{l=0}^{\infty} \epsilon(\boldsymbol{r}', \hat{\boldsymbol{v}}) e^{-\mu_t l} \; dl \tag{5.13}$$

We note that, the direction of emission from the source is equal to the direction of the light coming directly from the source (non-scattered light).

- $B(\boldsymbol{p}', \boldsymbol{p})$, is the kernel equal to,

$$B(\boldsymbol{p}', \boldsymbol{p}) = \mu_s \, p(\hat{\boldsymbol{v}}', \hat{\boldsymbol{v}}) \, e^{-\mu_t l} \tag{5.14}$$

5.2 Solution of the RTE for a homogeneous medium using Sequential Importance Sampling

Eq. (5.11) is a Fredholm integral equation of the second kind, hence, we could estimate the inner product of $I(\boldsymbol{p})$ with a weighting function $h(\boldsymbol{p})$ using Monte Carlo as explained in section 4.2.

Let, the quantity of interest be, Q, equal to,

$$Q = \iint I(\boldsymbol{r}, \hat{\boldsymbol{v}}) \, h(\boldsymbol{r}, \hat{\boldsymbol{v}}) d\boldsymbol{r} \, d\hat{\boldsymbol{v}} \tag{5.15}$$

By expanding, $I(\boldsymbol{r}, \hat{\boldsymbol{v}})$, using the Neumann's expansion, we could approximate Q, by the first K terms in the series,

$$Q \cong \sum_{k=1}^{K} \left(\iint \epsilon(\boldsymbol{r}_0, \hat{\boldsymbol{v}}_1) \, e^{-\mu_t l_1} \prod_{i=1}^{i=k} B(\boldsymbol{p}_{i-1}, \boldsymbol{p}_i) \, h(\boldsymbol{p}_k) \, d\boldsymbol{r}_0 d\hat{\boldsymbol{v}}_{1:k} \, dl_{1:k} \right) \tag{5.16}$$

We note that, by definition, the phase function, $p(\hat{\boldsymbol{v}}', \hat{\boldsymbol{v}})$, is a probability distribution [3, 8]. It could be interpreted as the probability of propagating in the direction $\hat{\boldsymbol{v}}$ due to the scattering of a photon incident in direction $\hat{\boldsymbol{v}}'$ [3, 6, 8]. And, $f(l) = \mu_t \, e^{-\mu_t l}$, is an

exponential probability distribution, thus the distance, l, could be interpreted as an exponential random variable. Accordingly, the kernel, $B(\boldsymbol{p}', \boldsymbol{p})$, could be written as,

$$B(\boldsymbol{p}', \boldsymbol{p}) = \frac{\mu_s}{\mu_t} T(\boldsymbol{p}', \boldsymbol{p}) \tag{5.17}$$

such that, $T(\boldsymbol{p}', \boldsymbol{p}) = p(\hat{\boldsymbol{v}}', \hat{\boldsymbol{v}}) f(l)$, is a transition kernel. And, $\tilde{\epsilon}(\boldsymbol{p})$, could be written as,

$$\tilde{\epsilon}(\boldsymbol{p}_1) = \frac{1}{\mu_t} \int_{l=0}^{\infty} \epsilon(\boldsymbol{r}_0, \hat{\boldsymbol{v}}_1) f(l)\, dl \tag{5.18}$$

Then, Eq. (5.16) could be written as

$$Q \cong \sum_{k=1}^{K} \left(\frac{1}{\mu_t} \left(\frac{\mu_s}{\mu_t} \right)^{k-1} \iint \epsilon(\boldsymbol{r}_0, \hat{\boldsymbol{v}}_1) f(l_1) \prod_{i=1}^{i=k} T(\boldsymbol{p}_{i-1}, \boldsymbol{p}_i)\, h(\boldsymbol{p}_k)\, d\boldsymbol{r}_0 d\hat{\boldsymbol{v}}_{1:k}\, dl_{1:k} \right) \tag{5.19}$$

such that, $\boldsymbol{r}_i = \boldsymbol{r}_{i-1} + l_i \hat{\boldsymbol{v}}_i$ for $i = 1, 2, \dots, k$.

The above equation could be solved using SIS, explained in section 4.2, by randomly sampling the radiation states. The first radiation state, $\boldsymbol{p}_1$, is sampled using two steps. First, we sample $(\boldsymbol{r}_0, \hat{\boldsymbol{v}}_1)$, the initial emission state from $\epsilon(\boldsymbol{p})$ (assuming that it is normalized, i.e., a probability distribution). Then, sample the distance, l_1, from $f(l)$, and calculate, $\boldsymbol{r}_1 = \boldsymbol{r}_0 + l_1 \hat{\boldsymbol{v}}_1$ (see Fig. (5.4)). The following radiation states $\{\boldsymbol{p}_i\}_{i=2:K}$, are sampled using the transition kernel, $T(\boldsymbol{p}', \boldsymbol{p}) = f(l) p(\hat{\boldsymbol{v}}', \hat{\boldsymbol{v}})$. To sample the i^{th} state, $\boldsymbol{p}_i \equiv (\boldsymbol{r}_i, \hat{\boldsymbol{v}}_i)$, from its previous state, $\boldsymbol{p}_{i-1}$, we first sample $\hat{\boldsymbol{v}}_i$ from the phase function, given that $\hat{\boldsymbol{v}}' = \hat{\boldsymbol{v}}_{i-1}$, i.e., sample $\hat{\boldsymbol{v}}_i$ from $p(\hat{\boldsymbol{v}} | \hat{\boldsymbol{v}}' = \hat{\boldsymbol{v}}_{i-1})$. Then, sample $\boldsymbol{r}_i$, through sampling the propagation distance l_i from $f(l)$, where, $\boldsymbol{r}_i = \boldsymbol{r}_{i-1} + l_i \hat{\boldsymbol{v}}_i$ (see Fig. (5.4)).

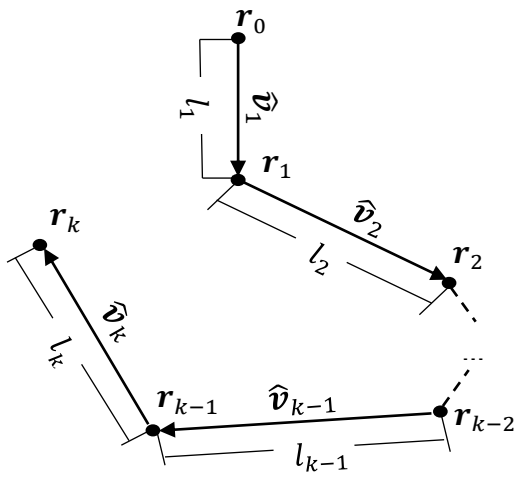

Figure 5.4 Updating radiation states (position and direction of propagation)

Using a large number, N, of samples of the radiation chain of states, $\{\boldsymbol{p}_i\}_{i=1:K}$, let the sample of the j^{th} chain be, $\left\{\boldsymbol{p}_i^{(j)}\right\}_{i=1:K}$, then, MC estimate of Q, is equal to,

$$\hat{Q} = \frac{1}{N}\sum_{k=1}^{K}\frac{1}{\mu_t}\left(\frac{\mu_s}{\mu_t}\right)^{k-1}\sum_{j=1}^{N} h\left(\boldsymbol{p}_k^{(j)}\right) \tag{5.20}$$

We note that, when using this sampling, the chains are independent of the weighting function $h(\boldsymbol{p})$. Therefore, we could use them to estimate several quantities of interest such as inner products with different $h(\boldsymbol{p})$ weighting functions.

For instance, consider the fluence at a position $\boldsymbol{r}$, given by,

$$\varphi(\boldsymbol{r}) = \int_{4\pi} I(\boldsymbol{r}, \hat{\boldsymbol{v}})\, d\hat{\boldsymbol{v}} \tag{5.21}$$

To estimate $\varphi(\boldsymbol{r})$ we use a weighting function that averages the fluence within a small volume, ΔV centered at $\boldsymbol{r}$. We could estimate the fluence at a set of positions $\{\boldsymbol{r}_i\}$, using the weighting functions,

$$h_i(\boldsymbol{r}, \hat{\boldsymbol{v}}) = \frac{\mathbb{1}_{\boldsymbol{r}_i}(\boldsymbol{r})}{\Delta V} \tag{5.22}$$

such that, $\mathbb{1}_{\boldsymbol{r}_i}(\boldsymbol{r})$ is an indicator function for the position, defined as,

$$\mathbb{1}_{\boldsymbol{r}_i}(\boldsymbol{r}) := \begin{cases} 1 & \boldsymbol{r} \in (\Delta V \text{ at } \boldsymbol{r}_i) \\ 0 & \boldsymbol{r} \notin (\Delta V \text{ at } \boldsymbol{r}_i) \end{cases} \tag{5.23}$$

Then, the MC estimate of the fluence at $\boldsymbol{r}_i$ is,

$$\hat{\varphi}(\boldsymbol{r}_i) = \frac{1}{N\Delta V} \sum_{k=1}^{K} \frac{1}{\mu_t} \left(\frac{\mu_s}{\mu_t}\right)^{k-1} \sum_{j=1}^{N} \mathbb{1}_{\boldsymbol{r}_i}\left(\boldsymbol{r}_k^{(j)}\right) \tag{5.24}$$

5.3 Mapping the RTE solution to Monte Carlo simulation of light

To map the solution derived to MC simulation procedure, we explain a basic MC simulation procedure for light propagation in homogeneous turbid media [18, 19]. To record the physical quantities of interest during the simulation, a grid system is created to enable the characterization of the local energy absorbed in the medium.

In summary, the steps for simulating the propagation of light emitted in direction $\hat{\boldsymbol{v}}_\epsilon$ from a source located at $\boldsymbol{r}_\epsilon$ are:

1. Launch a photon packet with weight, $W_0 = 1$, from the source.

$$\boldsymbol{r}_0 = \boldsymbol{r}_\epsilon, \qquad \hat{\boldsymbol{v}}_1 = \hat{\boldsymbol{v}}_\epsilon \tag{5.25}$$

2. Propagate the k^{th} step in the medium ($k = 1, 2, \dots$)
    a. Sample a propagation distance l_k from the exponential distribution, $f(l) = \mu_t \, e^{-\mu_t l}$.
    b. Propagate to the k^{th} interaction site,

$$\boldsymbol{r}_k = \boldsymbol{r}_{k-1} + l_k . \hat{\boldsymbol{v}}_k \tag{5.26}$$

    c. Calculate weight lost due to absorption,

$$\Delta W_k = \frac{\mu_a}{\mu_t} W_{k-1} \tag{5.27}$$

d. Accumulate the weight ΔW_k to the local grid element,

$$A(\boldsymbol{r}_k) = A(\boldsymbol{r}_k) + \Delta W_k \tag{5.28}$$

e. Calculate the new weight of the photon packet after absorption,

$$W_k = W_{k-1} - \Delta W_k = \frac{\mu_s}{\mu_t} W_{k-1} = \left(\frac{\mu_s}{\mu_t}\right)^k \tag{5.29}$$

f. Decide whether the packet will continue propagation or not. This could be decided according to a maximum value for k (equivalently a minimum value for W_k). If the packet continues propagation,

   i. Sample a new propagation direction $\hat{\boldsymbol{v}}_{k+1}$ from $p(\hat{\boldsymbol{v}}|\hat{\boldsymbol{v}}' = \hat{\boldsymbol{v}}_k)$.

   ii. Propagate the next step (repeat from step a)

3. Repeat the photon packet tracing from step 1 for a large number, N, of photon packets.

4. Estimate different quantities of interest,

   a. Absorbed photons per unit volume, at each grid positions ($\boldsymbol{r}_i$),

$$A(\boldsymbol{r}_i) = \frac{A(\boldsymbol{r}_i)}{N.\Delta V} \qquad (\text{cm}^{-3}) \tag{5.30}$$

   such that ΔV is the volume of the grid element.

   b. Photons fluence,

$$\hat{\varphi}(\boldsymbol{r}_i) = \frac{A(\boldsymbol{r}_i)}{\mu_a} \qquad (\text{cm}^{-2}) \tag{5.31}$$

From Eq. (5.27), and Eq. (5.29), the updating equation for the absorption, Eq. (5.28) could be written as

$$A(\boldsymbol{r}_k) = A(\boldsymbol{r}_k) + \frac{\mu_a}{\mu_t}\left(\frac{\mu_s}{\mu_t}\right)^{k-1} \tag{5.32}$$

Let the stopping criteria for the photon packet tracing be the number of steps, $k = K$. Then, the estimate of the fluence at a grid position $\boldsymbol{r}_i$, could be written as,

$$\hat{\varphi}(\boldsymbol{r}_i) = \frac{1}{N\Delta V}\left(\frac{1}{\mu_t}\right)\sum_{j=1}^{N}\sum_{k=1}^{K}\left(\frac{\mu_s}{\mu_t}\right)^{k-1} \mathbb{1}_{\boldsymbol{r}_i}\left(\boldsymbol{r}_k^{(j)}\right) \tag{5.33}$$

where, $\boldsymbol{r}_k^{(j)}$ is the k^{th} sampled position for the j^{th} simulated photon packet, and $\mathbb{1}_{\boldsymbol{r}_i}(\boldsymbol{r})$ is an indicator function for the position, given by Eq. (5.24).

It is clear the equivalence between the simulation procedure and the Sequential MC solution of the RTE. The update schema for the radiation states in the solution of the RTE and the simulation procedure are equivalent (shown in Fig. (5.4)). The source used in the simulation could be written as, $\epsilon(\boldsymbol{p}) = \delta(\boldsymbol{p} - \boldsymbol{p}_\epsilon)$, which is equivalent to having a deterministic source emission state. Moreover, the equations that estimate the fluence using both methods, Eq. (5.33) and Eq. (5.24), are equal.

Chapter 6

Simulation of the OCT signals using a finite probing area

We simulate the OCT signals (A-scans) using a finite beam incident on the surface of an inhomogeneous medium. The medium is constituted of arbitrarily shaped regions of different optical properties. Each region is defined by the following parameters: scattering coefficient μ_s, absorption coefficient μ_a, refractive index n, and anisotropy factor g. An optical fiber, of diameter Φ_f and acceptance angle θ_f, is placed above the medium surface by a distance 'd' (parallel to the medium surface), probing the medium by a beam of diameter Φ_p(see Fig. (6.1)). The direction of incidence on the medium surface, and the probing diameter Φ_p are calculated based on θ_f and Φ_f (see Fig. (6.1)).

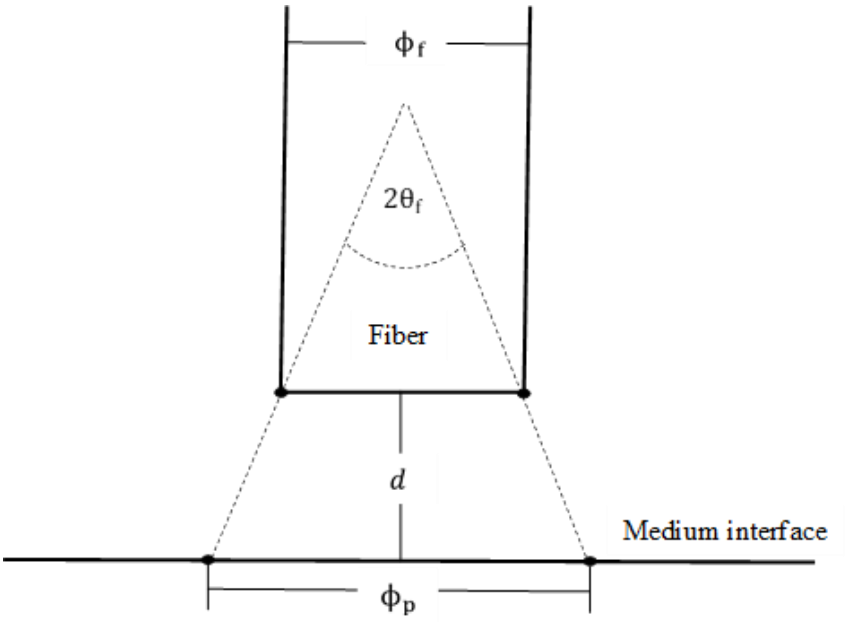

Figure 6.1. OCT fiber probe setup.

As mentioned earlier, there are two approaches to simulate the OCT signals (A-scans) due to a finite probing area. The first is the computationally costly superposition approach,

where the simulation of an infinitely-thin incident beam is repeated at different positions covering the probe area, then the finite beam signal is approximated by a weighted sum of thin beams signals (see section 6.1). The second is following the analytical solution of the RTE, the Sequential MC approach, where the incidence position of each photon packet is randomly sampled according to the intensity profile at the surface (see section 6.2).

In both approaches, photon packets are launched into the medium. The launch positions are set differently, and the total number of used photon packets would be different in both methods to achieve comparable accuracy. However, the simulation of packet propagation in the medium, and the biasing towards the fiber probe (importance sampling schema), and estimation of OCT signals (A-scans) from the reflected packets, are identical to ones used in OCT-MPS, see section 3.2.1 for more details.

Let $\underline{\mathrm{g}}(x_0, y_0)$ be the simulated OCT A-scan (Class I or Class II reflectance from different depths), due to a unit power, infinitely-thin beam incident at the position (x_0, y_0), i.e., the under bar notation in $\underline{\mathrm{g}}(x_0, y_0)$ signifies that it is a function of the depth z. The A-scan $\underline{\mathrm{g}}(x_0, y_0)$ is equal to the expected value of back-reflected power collected by the fiber (Class I or Class II) for each depth, given the position of the incident beam, it could be written as,

$$\underline{\mathrm{g}}(x_0, y_0) = \mathbf{E}\{\underline{w}_r | x_0, y_0\} \tag{6.1}$$

such that, $\underline{w}_r$ is the weight, from each depth, of the collected photon packet (Class I or Class II portion of the photon packet).

To estimate $\underline{\mathrm{g}}(x_0, y_0)$ using MC, a large number (N_g) of photon packets are launched from (x_0, y_0) and propagated in the medium to get samples of $\underline{w_r}$. Then, MC estimate of $\underline{\mathrm{g}}(x_0, y_0)$ is the mean of the samples of $\underline{w_r}$, and the error in the estimate is given by,

$$\left|\underline{e_g}\right| \cong \frac{\underline{\sigma_g}}{\sqrt{N_g}} \tag{6.2}$$

such that, $\underline{\sigma_g^2} \equiv \mathbf{var}\{\underline{w_r}|x_0, y_0\}$ is the variance of the weight collected by the fiber from all depths. It is important to note that we will assume that $\underline{\sigma_g^2}$ is approximately equal over the support of the incident beam, i.e., $\underline{\sigma_g^2}$ would be assumed to not depend on (x_0, y_0).

6.1 Superposition approach for simulating a finite incident beam

Assume that the surface of the medium is in the XY-plane, i.e., $z = 0$, and normal to the z-axis. Let, $\epsilon(x_0, y_0)$, be a function that defines the finite incident beam profile, then the OCT signal due to the finite beam, denoted as $\underline{\mathrm{R}}$, is given by the superposition integral,

$$\underline{\mathrm{R}} = \iint \epsilon(x_0, y_0)\, \underline{\mathrm{g}}(x_0, y_0)\, dxdy \tag{6.3}$$

In this approach, we focus on solving the superposition integral above by any quadrature method. We use the composite midpoint quadrature rule as a basic superposition method to compare between both approaches, even though other possible quadrature rules that could be used.

The composite midpoint quadrature rule approximation of a one-dimensional integral is given by,

$$I = \int_a^b f(x)\,dx = h_x \sum_{i=1}^{M_x} f\left(x^{(i)}\right) + e_q \tag{6.4}$$

where, $x^{(i)}$, are the quadrature nodes (points), given by,

$$x^{(i)} = a + \left(i - \frac{1}{2}\right) h_x\,, \qquad i = 1, 2, \dots, M_x \tag{6.5}$$

the quadrature weights are constant, equal to,

$$h_x = \frac{b-a}{M_x} \tag{6.6}$$

and, e_q, is the quadrature error, given by [44, 45],

$$\left|e_q\right| \leq \frac{(b-a)}{24}\, h_x^2\, \max|f''(x)| \tag{6.7}$$

The order of the error, e_q, is $O(h_x^2)$, which is equivalent to $O(M_x^{-2})$.

The composite midpoint quadrature rule could also be extended to double integrals,

$$I = \iint_A f(x,y)\,dx\,dy = \int_a^b \int_{c(x)}^{d(x)} f(x,y)\,dy\,dx \tag{6.8}$$

The integral above could be written as,

$$I = \int_a^b F(x)\,dx \tag{6.9}$$

where,

$$F(x) = \int_{c(x)}^{d(x)} f(x,y)\,dy \tag{6.10}$$

First, by approximating Eq. (6.9) using the composite midpoint rule (Eq. (6.5) and Eq. (6.6) gives the quadrature nodes and weights). Then, by approximating Eq. (6.10) using the composite midpoint rule, where

$$h_y^{(i)} = \frac{d(x^{(i)}) - c(x^{(i)})}{M_y^{(i)}} \tag{6.11}$$

and,

$$y^{(i,j)} = c\left(x^{(i)}\right) + \left(j - \frac{1}{2}\right) h_y^{(i)}, \qquad j = 1, 2, \dots, M_y^{(i)} \tag{6.12}$$

Eq. (6.8) is approximated by,

$$I = \sum_{i=1}^{M_x} \sum_{j=1}^{M_y^{(i)}} h_x \, h_y^{(i)} \, f\left(x^{(i)}, y^{(i,j)}\right) + e_q \tag{6.13}$$

where the order of the error, e_q, is given by $O\left(h_x^2 + \max_i \left\{ {h_y^{(i)}}^2 \right\}\right)$.

When we implemented this simulation approach, we used a user-defined maximum distance, h_{max}, between any two adjacent nodes (in X or Y direction), to calculate M_x, $M_y^{(i)}$ and the quadrature nodes accordingly. First, the number of grid lines in the X direction is calculated according to,

$$M_x = \left\lceil \frac{b - a}{h_{max}} \right\rceil \tag{6.14}$$

such that, $\lceil \cdot \rceil$ is the ceiling function. Then, h_x and $x^{(i)}$ are calculated from equations (6.6) and (6.5) respectively. Following that, for each grid line in the X direction, the number of grid lines in the Y direction are calculated according to,

$$M_y^{(i)} = \left\lceil \frac{d(x^{(i)}) - c(x^{(i)})}{h_{max}} \right\rceil \tag{6.15}$$

Then, $h_y^{(i)}$ and $y^{(i,j)}$ are calculated from equations (6.11) and (6.12), i.e., the grid lines in the Y direction are not uniform.

Eq. (6.13) could be written in a compact form as,

$$I = \sum_{m=1}^{M} h^{(m)} f\left(x^{(m)}, y^{(m)}\right) + e_q \tag{6.16}$$

where, $m \equiv (i,j)$, $h^{(m)} = h_x . h_y^{(i)}$, and M is the total number of quadrature nodes.

By applying the composite midpoint rule to the superposition integral in Eq. (6.3) (assuming that it is a definite integral) we get,

$$\underline{\mathrm{R}} = \sum_{m=1}^{M} h^{(m)} \epsilon\left(x_0^{(m)}, y_0^{(m)}\right) \underline{\mathrm{g}}\left(x_0^{(m)}, y_0^{(m)}\right) + \underline{e}_q \tag{6.17}$$

where, $\left\{\left(x_0^{(m)}, y_0^{(m)}\right)\right\}$ are the quadrature nodes.

We note that each term, $\underline{\mathrm{g}}\left(x_0^{(m)}, y_0^{(m)}\right)$, in Eq. (6.17), should be estimated using a MC simulation using an infinitely thin beam. Denote the error in the estimate of $\underline{\mathrm{g}}\left(x_0^{(m)}, y_0^{(m)}\right)$ by $\underline{e}_g\left(x_0^{(m)}, y_0^{(m)}\right)$. Therefore, the total error in the estimate of $\underline{\mathrm{R}}$ is given by,

$$\underline{e}_R^{SP} \cong \sum_{m=1}^{M} h^{(m)} \epsilon\left(x_0^{(m)}, y_0^{(m)}\right) \underline{e}_g\left(x_0^{(m)}, y_0^{(m)}\right) + \underline{e}_q \tag{6.18}$$

The errors in the terms, $\left\{\underline{\mathrm{g}}\left(x_0^{(m)}, y_0^{(m)}\right)\right\}$ add in quadrature [46], so the error in $\underline{\mathrm{R}}$ becomes,

$$\left|\underline{e}_R^{SP}\right| \cong \sqrt{\sum_{m=1}^{M} {h^{(m)}}^2 \epsilon^2\left(x_0^{(m)}, y_0^{(m)}\right) \underline{e}_g^2\left(x_0^{(m)}, y_0^{(m)}\right)} + \left|\underline{e}_q\right| \tag{6.19}$$

The error, $\underline{e}_g\left(x_0^{(m)}, y_0^{(m)}\right)$, for each term is given by Eq. (6.2). Therefore, since we assumed that $\underline{e}_g^2\left(x_0^{(m)}, y_0^{(m)}\right)$ does not change from one quadrature node to another, we could write Eq. (6.19) as,

$$\left|\underline{e}_R^{(\mathrm{SP})}\right| \cong \frac{\sigma_g}{\sqrt{N_g}} \sqrt{\sum_{m=1}^{M} h^{(m)^2} \epsilon^2\left(x_0^{(m)}, y_0^{(m)}\right)} + \left|\underline{e}_q\right| \tag{6.20}$$

We note that that, for each quadrature point, we would need to run a simulation with N_g (large number) photon packets. Therefore, the total number of photon packets to be used in a superposition-based simulator would be $M.N_g$.

6.2 Sequential MC approach for simulating a finite incident beam

This approach is following the analytical solution of the RTE, described in section 5.2. The launch position of the photon packets is considered a random variable. The incident beam is defined by,

$$\epsilon(x_0, y_0) = \mathrm{P}_\epsilon \, f_\epsilon(x_0, y_0) \tag{6.21}$$

where $f_\epsilon(x_0, y_0)$ is a probability distribution function of the spatial distribution of the incident intensity at the surface of the medium, and $\mathrm{P}_\epsilon = \iint \epsilon(x_0, y_0)\, dx_0 dy_0$ is the total power in the beam. The OCT signal (A-scan), $\underline{\mathrm{R}}$, is equal to the expected value of back-reflected power from each depth, which could be written as,

$$\underline{\mathrm{R}} = \mathrm{P}_\epsilon \, \mathbf{E}\{\underline{w}_r\} \tag{6.22}$$

where $\underline{w}_r$ is the packet reflected weight from each depth.

According to the law of total expectation that is given by [47]

$$\mathbf{E}\{u\} = \mathbf{E}_{f_v}\{\mathbf{E}\{u|v\}\} \tag{6.23}$$

where f_v is the probability distribution of v. Defining $u \equiv \mathrm{P}_\epsilon \, \underline{w}_r$, and $v \equiv (x_0, y_0)$, then, $q_v = f_\epsilon(x_0, y_0)$ and,

$$\underline{\mathrm{R}} = \mathrm{P}_\epsilon \cdot \mathbf{E}\{\underline{w}_R\} = \mathrm{P}_\epsilon \, \mathbf{E}_{f_\epsilon}\left\{\mathbf{E}\{\underline{w}_r|x_0, y_0\}\right\} \tag{6.24}$$

Substituting Eq. (6.1) into (6.24) we obtain,

$$\underline{\mathrm{R}} = \mathrm{P}_\epsilon \cdot \mathbf{E}_{f_\epsilon}\left\{\underline{\mathrm{g}}(x_0, y_0)\right\} = \mathrm{P}_\epsilon \iint \underline{\mathrm{g}}(x_0, y_0)\, f_\epsilon(x_0, y_0) dx_0 dy_0 \tag{6.25}$$

which is identical to the superposition integral in Eq. (6.3), except that $\epsilon(x_0, y_0)$ that represents the spatial distribution of the finite beam, is now described by a probability distribution function rather than a deterministic function.

The reflectance, $\underline{\mathrm{R}}$, could be estimated using MC by simulating a large number (N) of photon packets to get samples of $\underline{w}_r$, where the launch position of each photon packet is randomly sampled from $f_\epsilon(x_0, y_0)$. Then, the estimate of $\underline{\mathrm{R}}$ is equal to the sample mean of $\underline{w}_r$ and the error in the estimate is given by,

$$\left|\underline{e}_R\right| \cong \frac{\underline{\sigma}_R}{\sqrt{N}} \tag{6.26}$$

where $\underline{\sigma}_R^2 \equiv \mathbf{var}\{\mathrm{P}_\epsilon \, \underline{w}_r\}$.

The randomness in the photons incidence position would increase the variance of $\underline{w}_r$ compared to the case when the position is deterministic (infinitely-thin beam). Therefore, to obtain a comparable accuracy, more photon packets may be needed in the finite beam case than those needed in the infinitely-thin beam case. Therefore, we analyze the variance introduced due to the randomness in the photon packet incidence positions.

The law of the total variance allows us to write the variance in the case of a finite incident beam, $\underline{\sigma}_R^2$, in terms of the variance $\underline{\sigma}_g^2(x_0, y_0)$ (variance in the case of a unit power infinitely-thin incident beam).

Recalling the law of total variance [48],

$$\mathbf{var}\{u\} = \mathbf{E}_{q_v}\{\mathbf{var}\{u|v\}\} + \mathbf{var}_{q_v}\{\mathbf{E}\{u|v\}\} \tag{6.27}$$

where f_v is the probability distribution of v. Defining $u \equiv \mathrm{P}_\epsilon\, \underline{w}_R$, and $v \equiv (x_0, y_0)$, then, $q_v = f_\epsilon(x_0, y_0)$. And,

$$\mathbf{var}\{\mathrm{P}_\epsilon\, \underline{w}_R\} = \mathrm{P}_\epsilon^2 \cdot \mathbf{E}_{f_\epsilon}\left\{\mathbf{var}\{\underline{w}_r|x_0, y_0\}\right\} + \mathrm{P}_\epsilon^2 \cdot \mathbf{var}_{f_\epsilon}\left\{\mathbf{E}\{\underline{w}_r|x_0, y_0\}\right\} \tag{6.28}$$

Therefore, from Eq. (6.1),

$$\underline{\sigma}_R^2 = \mathrm{P}_\epsilon^2\left(\mathbf{E}_{f_\epsilon}\{\underline{\sigma}_g^2(x_0, y_0)\} + \mathbf{var}_{f_\epsilon}\left\{\underline{\mathrm{g}}(x_0, y_0)\right\}\right) \tag{6.29}$$

Following the assumption that, $\underline{\sigma}_g^2(x_0, y_0)$ is constant over the support of the incident beam, Eq. (6.29) becomes,

$$\underline{\sigma}_R^2 = \mathrm{P}_\epsilon^2\left(\underline{\sigma}_g^2 + \mathbf{var}_{f_\epsilon}\left\{\underline{\mathrm{g}}(x_0, y_0)\right\}\right) \tag{6.30}$$

We note that $\underline{\sigma}_g^2$ in Eq. (6.30) results from the uncertainty due to the photon propagation in the turbid medium (a long random walk), while $\mathbf{var}_{f_\epsilon}\left\{\underline{\mathrm{g}}(x_0, y_0)\right\}$ results from the uncertainty due to the photon packet incidence positions. Therefore, the variance term, $\underline{\sigma}_g^2$, which depends on a long chain of random variables (radiation states), is typically much larger than the term, $\mathbf{var}_{f_\epsilon}\left\{\underline{\mathrm{g}}(x_0, y_0)\right\}$, which depends on one random variable (the initial position),

$$\underline{\sigma}_g^2 \gg \mathbf{var}_{f_\epsilon}\left\{\underline{\mathrm{g}}(x_0, y_0)\right\} \tag{6.31}$$

Eq. (6.30) will be approximately equal to,

$$\underline{\sigma}_R^2 \cong \mathrm{P}_\epsilon^2\, \underline{\sigma}_g^2 \tag{6.32}$$

and the error in the estimate could be written as,

$$\left|\underline{e}_{\mathrm{R}}^{(\mathrm{MC})}\right| \cong \frac{\mathrm{P}_{\epsilon}\,\underline{\sigma}_{g}}{\sqrt{N}} \tag{6.33}$$

6.3 Comparison between errors resulting from two simulation approaches

When using the superposition approach, the total number of packets is $M.N_g$ and the error is $\underline{e}_{\mathrm{R}}^{(\mathrm{SP})}$, which is given by Eq. (6.20). When using the Sequential MC approach, the total number of packets is N and the error is $\underline{e}_{\mathrm{R}}^{(\mathrm{MC})}$, which is given by Eq. (6.33). Below, we compare these two errors when the total number of photon packets used are equal, i.e., $N = M.N_g$, which would require comparable computational time.

Recalling the Cauchy Schwarz inequality [49],

$$|\langle u,v\rangle|^2 \leq \langle u,u\rangle\,.\langle v,v\rangle \tag{6.34}$$

Let $u[m] = 1$ and $v[m] = h^{(m)}\epsilon\left(x_0^{(m)}, y_0^{(m)}\right)$, with, $m = 1, 2, \ldots, M$, then,

$$|\langle u,v\rangle|^2 = \left(\sum_{m=1}^{M} 1\,.\,h^{(m)}\,\epsilon\left(x_0^{(m)}, y_0^{(m)}\right)\right)^2, \tag{6.35}$$

$$\langle u,u\rangle = \sum_{m=1}^{M} 1^2 = M, \tag{6.36}$$

$$\langle v,v\rangle = \sum_{m=1}^{M}\left(h^{(m)}\,\epsilon\left(x_0^{(m)}, y_0^{(m)}\right)\right)^2 = \sum_{m=1}^{M} {h^{(m)}}^2\,\epsilon^2\left(x_0^{(m)}, y_0^{(m)}\right). \tag{6.37}$$

Therefore,

$$\left(\sum_{m=1}^{M} h^{(m)}\,\epsilon\left(x_0^{(m)}, y_0^{(m)}\right)\right)^2 \leq M\sum_{m=1}^{M} {h^{(m)}}^2\,\epsilon^2\left(x_0^{(m)}, y_0^{(m)}\right) \tag{6.38}$$

We note that, P_{ϵ}, is approximately equal to,

$$\mathrm{P}_{\epsilon} = \iint \epsilon(x_0, y_0)\, dx_0 dy_0 \cong \sum_{m=1}^{M} h^{(m)}\, \epsilon\left(x_0^{(m)}, y_0^{(m)}\right) \tag{6.39}$$

Therefore, Eq. (6.38) is approximately equal to,

$$\frac{\mathrm{P}_{\epsilon}}{\sqrt{M}} \leq \sqrt{\sum_{m=1}^{M} {h^{(m)}}^2\, \epsilon^2\left(x_0^{(m)}, y_0^{(m)}\right)} \tag{6.40}$$

By multiplying Eq. (6.40) by $\frac{\sigma_g}{\sqrt{N_g}}$, we obtain,

$$\frac{\sigma_g}{\sqrt{N_g}} \frac{\mathrm{P}_{\epsilon}}{\sqrt{M}} \leq \frac{\sigma_g}{\sqrt{N_g}} \sqrt{\sum_{m=1}^{M} {h^{(m)}}^2\, \epsilon^2\left(x_0^{(m)}, y_0^{(m)}\right)} \tag{6.41}$$

The left-hand side of Eq. (6.41) is equal to $\underline{e}_{\mathrm{R}}^{(\mathrm{MC})}$ in Eq. (6.33), and the right-hand side of Eq. (6.41) is equal to $\left(\left|\underline{e}_{\mathrm{R}}^{(\mathrm{SP})}\right| - \left|\underline{e}_q\right|\right)$ in Eq. (6.20). Therefore, (6.41) becomes,

$$\left|\underline{e}_{\mathrm{R}}^{(\mathrm{MC})}\right| \leq \left|\underline{e}_{\mathrm{R}}^{(\mathrm{SP})}\right| - \left|\underline{e}_q\right| \tag{6.42}$$

Eq. (6.42) indicates that, for an equal number of packets, the error in the OCT signal calculation obtained using the Sequential MC approach is smaller than the corresponding error obtained when using the superposition approach.

In the superposition approach, M (the number of quadrature points) is chosen to reach an acceptable quadrature error $\underline{e}_q$. Therefore, M may be large, and the total number of packets, $M.N_g$, may not be practical. On the other hand, when using the Sequential MC approach, there is no quadrature error. Therefore, N (the number of packets) is chosen flexibly according to the desired accuracy. Another advantage of using the Sequential MC approach

is the ability to estimate the error by calculating the variance. However, in the superposition method, the function $\underline{g}(x_0, y_0)$ in the integrand is unknown and, as a consequence, one cannot accurately estimate the quadrature error.

6.4 Implementation and Numerical Results

We chose the Sequential MC approach to implement our finite beam OCT simulator because of its superior performance when compared with the superposition simulation approach. We also implemented a superposition-based MC simulator to validate the results of our simulator. Both simulators are implemented in NVIDIA's CUDA environment using extensions of the C language; their codes are based on the OCT-MPS code.

For the distribution of the light intensity at the surface of the medium, we considered a bivariate normal distribution with standard deviation equal to, $\frac{\Phi_p}{6}$, i.e., the probing area contains 99% of the incident power. The superposition-based simulator is implemented according to the composite midpoint quadrature rule (as described in section 6.1). For the Sequential MC based simulator, we created an independent stream of pseudo-random numbers to sample the photon packet launch position. The launch position of the photon packet is sampled from the bivariate normal distribution using the Box-Muller method. Following this method, the incidence position, (x_0, y_0), on the surface of the medium is given by [35],

$$x_0 = x_f + \frac{\Phi_p}{6}\sqrt{-2\ln(u_1)}\cos(2\pi\, u_2) \tag{6.43}$$

$$y_0 = y_f + \frac{\Phi_p}{6}\sqrt{-2\ln(u_1)}\sin(2\pi\, u_2) \tag{6.44}$$

where (x_f, y_f) is the fiber probe center position, and u_1, u_2 are uniform random variables over the interval $[0, 1]$.

We simulated the OCT signals from two different inhomogeneous media, (a) a slab containing two spheres and a tri-axial ellipsoid, (b) a slab containing a tri-axial ellipsoid. In both cases, we used an optical source of unit power and coherence length l_c = 15 μm, a fiber probe of diameter Φ_f = 20 μm and acceptance angle θ_f = 5°. The fiber is placed above the medium by a distance, d = 0.25 mm, which means that the probing diameter at the surface of the medium $\Phi_p \cong 64$ μm. The configuration of the implemented importance sampling is the same as in [24, 25] (a = 0.925, and p = 0.5).

All the results reported are obtained using a workstation with the NVIDIA Tesla P100-12GB graphics processing unit (GPU) with compute capability 6.0. The P100 GPU is built in the Pascal architecture, which has 56 streaming multiprocessors (SMs) with 64 CUDA cores each (a total of 3584 cores) running at 1328 MHz. The GPU has 12GB of memory (HBM2) with 549 GB/s peak memory bandwidth.

6.4.1 Simulation Case 1

The abstract view of the medium is shown in Fig. (6.2). The medium has a square surface of side length 3 mm (centered at the origin in the XY-plane), and its thickness is 1 mm (in the z-axis). The spheres have a 0.06 mm radius, and are centered at, (0.08, 0.0, 0.1) mm, (-0.08, 0.0, 0.3) mm. The tri-axial ellipsoid is centered at, (0.0, 0.0, 0.2) mm, and its axes are represented by, v_1 = [0.06 sin(60°), 0, -0.06 cos(60°)]^T mm, v_2 = [0, 1, 0]^T mm, and v_3 = [0.17 sin(30°), 0, 0.17 cos(30°)]^T mm.

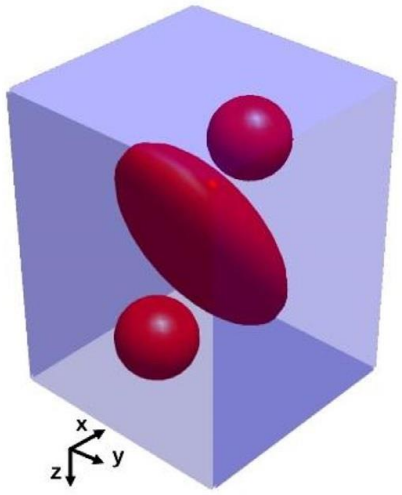

Figure 6.2. Abstract view of the medium: a slab containing an Ellipsoid and two spheres

The optical parameters of the medium are shown in Table (6.1). The tetrahedron mesh of this medium is shown in Fig. (6.3), it has a total of 5248 vertices and 29,697 tetrahedrons, it was generated by NETGEN [50].

Table 6.1. Optical parameters of the medium: a slab containing an Ellipsoid and two spheres

	'μ_a' (cm^{-1}) Absorption coefficient	'μ_s' (cm^{-1}) Scattering coefficient	'g' Anisotropy factor	'n' Refractive index
Background	1.5	60	0.9	1
Spheres	3	120	0.9	1
Ellipsoid	3	120	0.9	1

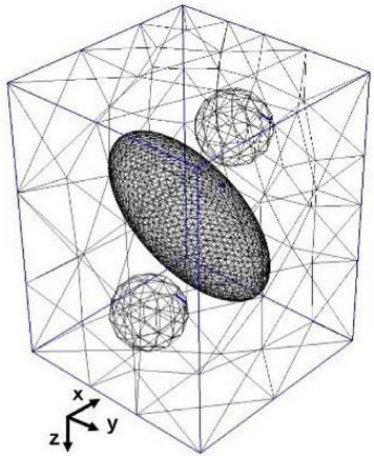

Figure 6.3. Tetrahedron mesh of the medium: a slab containing an Ellipsoid and two spheres

Similar to other MC simulators, the accuracy of our simulator is given by the confidence interval (CI) of its estimate, equal to,

$$\underline{\mathrm{CI}} \equiv \left[\underline{\hat{\mathrm{R}}} - \underline{\widehat{e_R}}\,,\, \underline{\hat{\mathrm{R}}} + \underline{\widehat{e_R}}\right] \tag{6.45}$$

such that, $\underline{\hat{\mathrm{R}}}$ is the estimate of the A-scan (Class I or Class II), and $\underline{\widehat{e_R}}$ is the estimate of the error in $\underline{\hat{\mathrm{R}}}$.

6.4.1.1 Validation of our finite beam simulator with a superposition-based simulator

First, we consider using the superposition-based simulator to estimate an A-scan of Class I reflectivity, at the lateral position $x = -0.1$ mm, due to a finite incident beam with a Gaussian intensity profile. The quadrature nodes are set according to a defined maximum distance, h_{max}, between any two quadrature nodes (in X or Y direction) as explained in section (6.1). For an acceptable error in the estimate of $\underline{\mathrm{g}}(x_0, y_0)$ (A-scan due to an infinitely-thin incident beam at position x_0, y_0) the number of photon packets used to estimate it is $N_g = 10^7$ (as reported by Malektaji in [25]). To choose h_{max}, several calculations decreasing the value of h_{max}, i.e., increasing the number of quadrature nodes

M, were carried until the A-scan converge (see Fig. (6.4)). Fig. (6.4) shows that the A-scan at this lateral position converges when using the distance h_{max} = 4 μm.

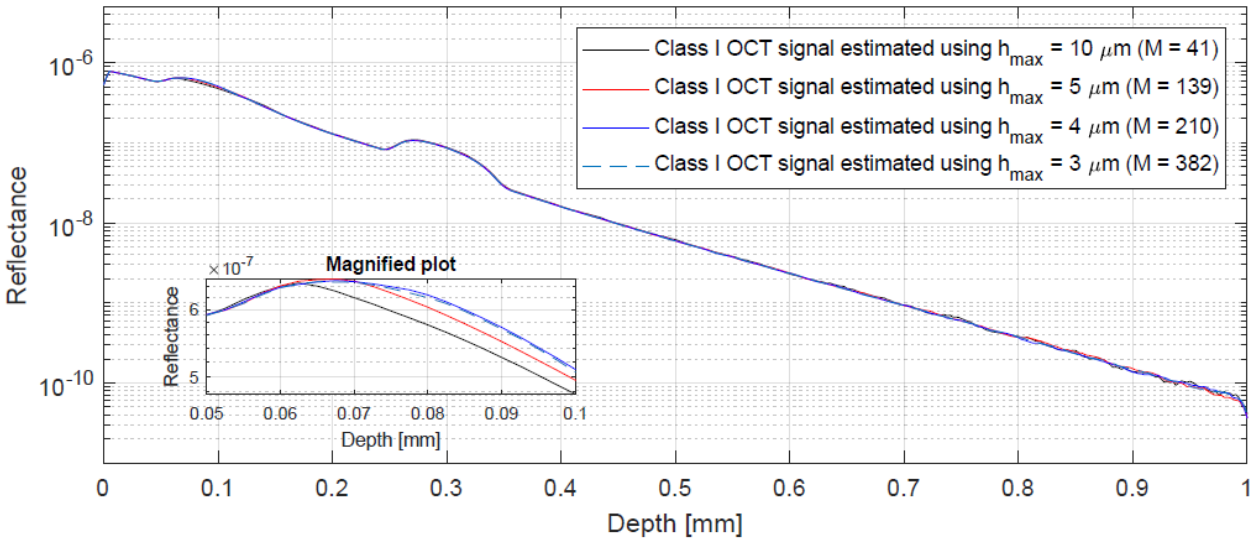

Figure 6.4. Class I signal A-scan, at the lateral position $x = -0.1$ mm, due to a finite incident beam with a Gaussian intensity profile, obtained using the superposition-based simulator with different numbers of quadrature nodes (M).

We validate the results of our Sequential MC based simulator with those obtained using the superposition-based simulator (when h_{max} = 4 μm, i.e., using 210 quadrature point). Figs. (6.5) and (6.6) show the A-scan of Class I and Class II reflectivity, respectively, obtained using the superposition-based simulator and our Sequential MC based simulator. When using our simulator, the number of photon packets needed to reach an acceptable error was N =10^7. The confidence intervals of the estimates of our simulator are calculated and shown on both figures at different depths.

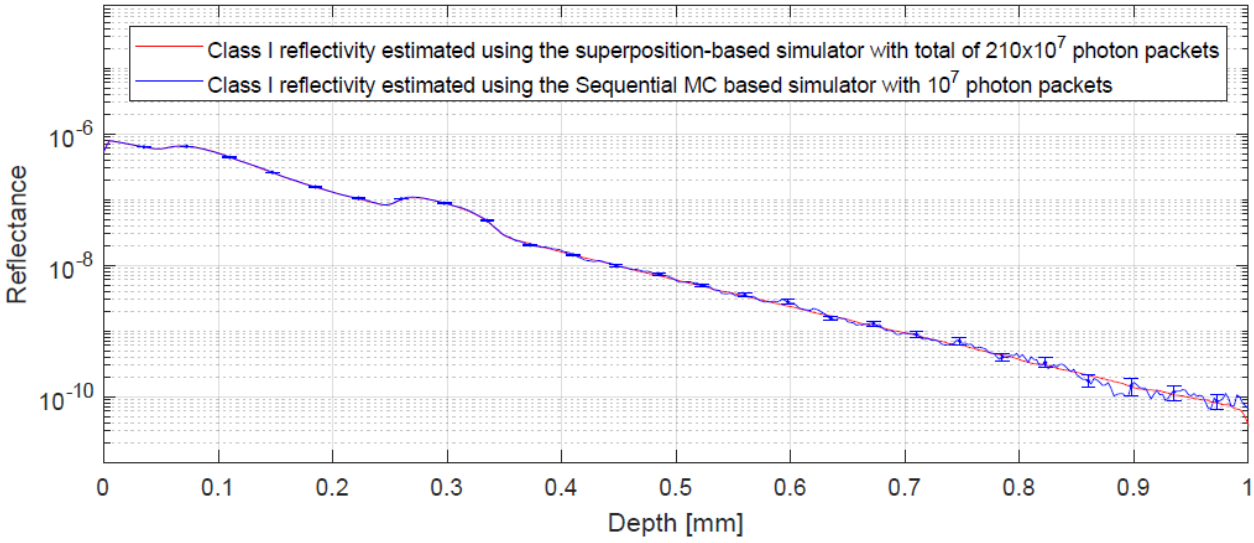

Figure 6.5. Comparison of finite beam A-scan of Class I reflectivity estimated using: superposition-based simulator with a total of 210×10^7 photon packets (210 quadrature nodes, plotted in red), and our Sequential MC based simulator with 10^7 photon packets (plotted in blue, showing confidence interval at different depths).

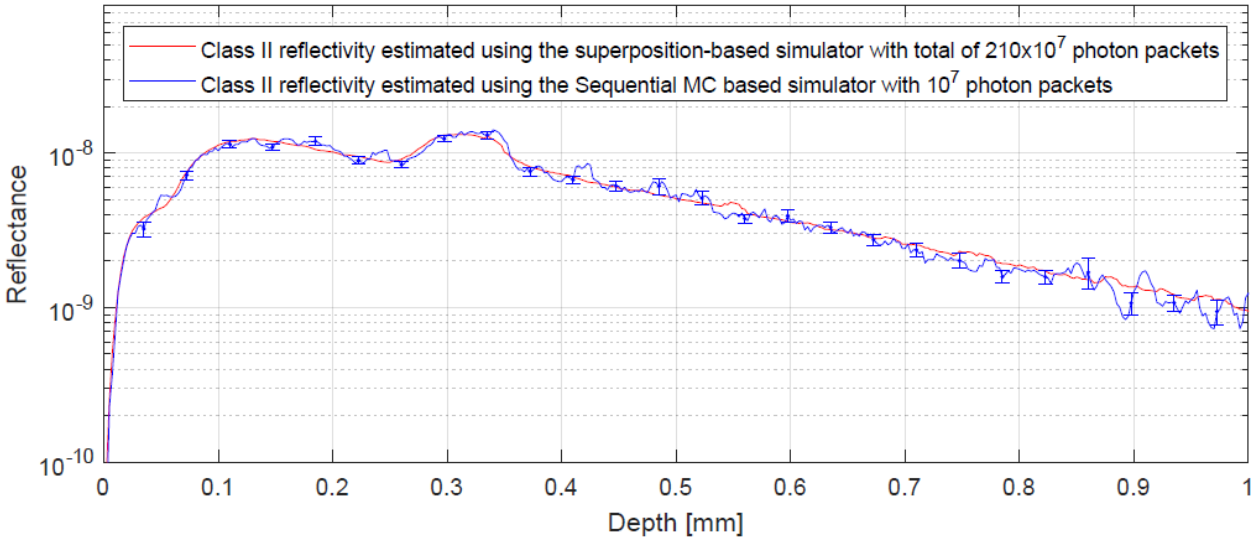

Figure 6.6. Comparison of finite beam A-scan of Class II reflectivity estimated using: superposition-based simulator with a total of 210×10^7 photon packets (210 quadrature nodes, plotted in red), and our Sequential MC based simulator with 10^7 photon packets (plotted in blue, showing confidence interval at different depths).

Figs. (6.5) and (6.6) show that the results obtained using both simulators are in agreement. The number of photon packets needed by any of the simulators is proportional to its computational time. The number of photon packets used by our simulator was 10^7, and the

computation time was 8.5 seconds. The total number of packets used by the superposition-based simulator was 210×10^7 (210 quadrature point each simulated by 10^7 photon packets), and the total time was 30 minutes.

6.4.1.2 Error comparison and analysis between our Sequential MC based simulator and the superposition-based simulator

Assume that, when using a large number of quadrature nodes the quadrature error $\underline{e}_q$ is negligible. Then, from Eq. (6.19) the error of superposition-based simulator could be estimated according to,

$$\left|\underline{\hat{e}}_{\mathrm{R}}^{(\mathrm{SP})}\right| \cong \sqrt{\sum_{m=1}^{M} {h^{(m)}}^2 \epsilon^2\left(x_0^{(m)}, y_0^{(m)}\right)\ \underline{\hat{e}}_{\underline{g}}^2\left(x_0^{(m)}, y_0^{(m)}\right)} \tag{6.46}$$

such that, $\underline{\hat{e}}_g\left(x_0^{(m)}, y_0^{(m)}\right)$, is the estimate of the error in $\underline{\hat{\mathrm{g}}}\left(x_0^{(m)}, y_0^{(m)}\right)$.

We compare the errors of both simulators for the A-scan simulated above. From Fig. (6.4), we assume that the quadrature error is negligible when using 210 quadrature nodes. First we compare the errors when using our Sequential MC based simulator with 10^7 photon packets. Figs. (6.7) and (6.8) compares the estimated errors of both simulators estimates of Class I and Class II reflectivity, respectively. As expected, the superposition-based simulator results are more accurate since the total number of photon packets this simulator used was 210 times more than those used by our simulator. However, in the superposition-based simulator, if we reduce the total number of packets by reducing the number of quadrature nodes, the quadrature error ($\underline{e}_q$) may be significant as illustrated in Fig. (6.4).

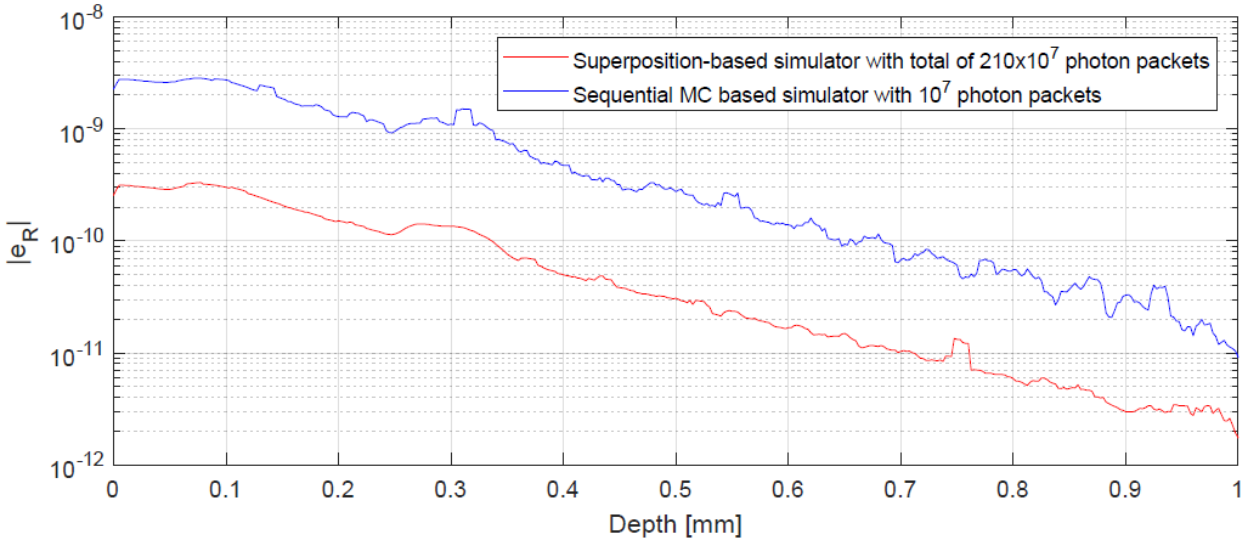

Figure 6.7. Comparison of error in the estimate of Class I reflectivity estimated using: superposition-based simulator with a total of 210×10^7 photon packets (210 quadrature nodes, plotted in red), and our Sequential MC based simulator with 10^7 photon packets (plotted in blue).

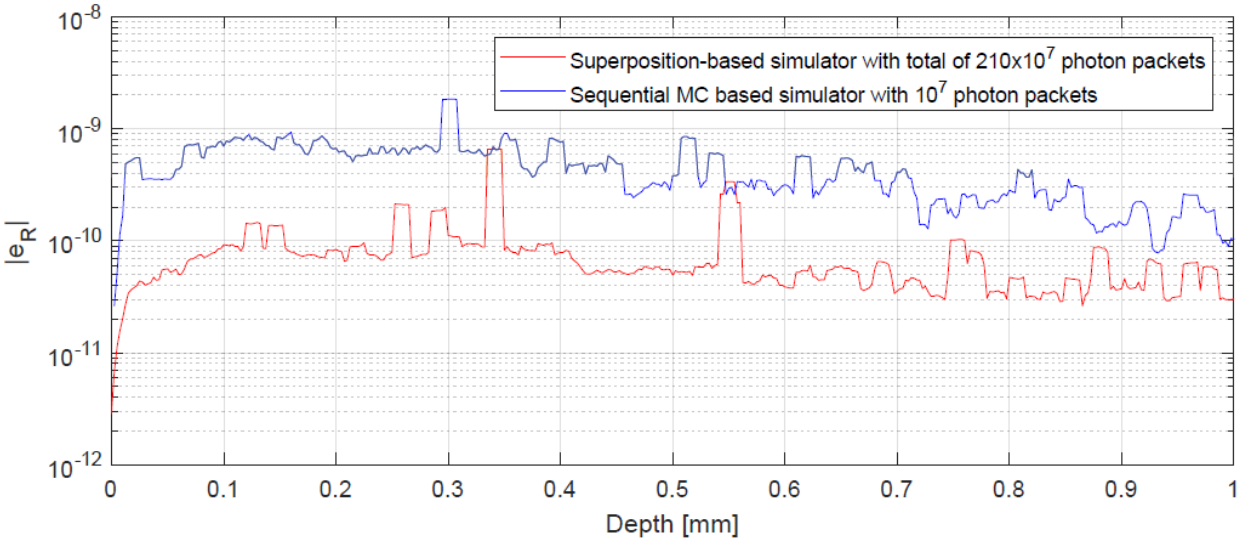

Figure 6.8. Comparison of error in the estimate of Class II reflectivity estimated using: superposition-based simulator with a total of 210×10^7 photon packets (210 quadrature nodes, plotted in red), and our Sequential MC based simulator with 10^7 photon packets (plotted in blue).

Second, we compare the results of both simulators when they have comparable computational cost, i.e., $N = M.N_g$. We reran our simulator with N = 210×10^7 photon packets (equal to the total number of photon packets used by the superposition-based

simulator), the computation time was 30 minutes. Figs. (6.9) and (6.10) compare both simulators estimated Class I and Class II reflectivity, respectively. Figs. (6.11) and (6.12) compare both simulators estimated errors for Class I and Class II reflectivity estimates, respectively. Fig. (6.11) shows that, for Class I reflectivity, at a comparable computational cost the estimated error of the Sequential MC based simulator estimate was smaller than that of the superposition-based simulator estimate at all depths. Fig. (6.12) shows that, for Class II reflectivity, at a comparable computational cost the estimated error of the Sequential MC based simulator estimate was on average smaller than that of the superposition-based simulator estimate.

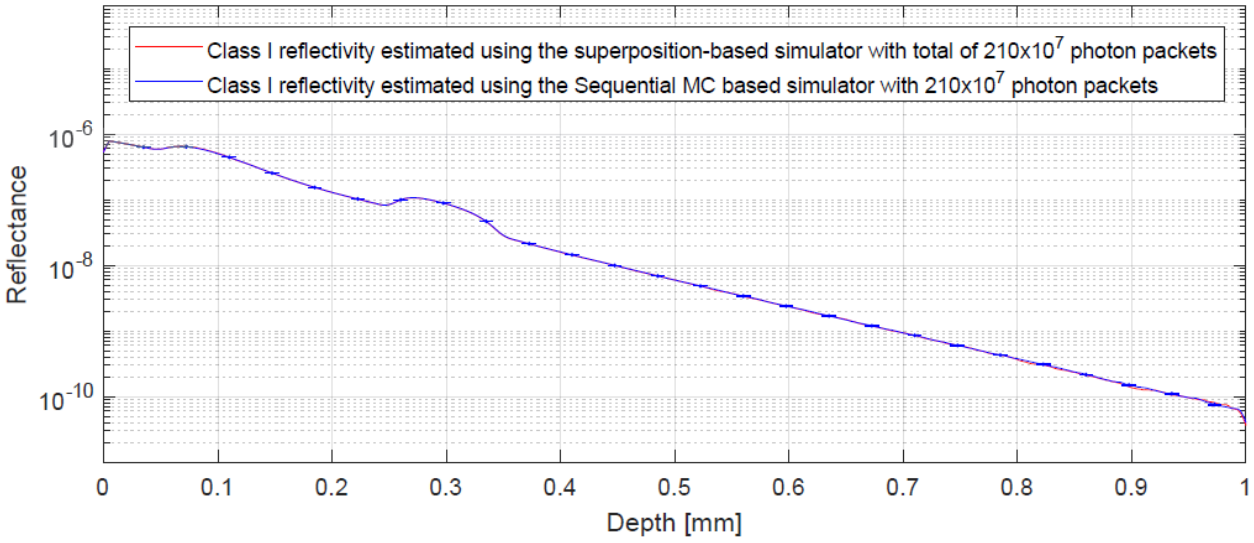

Figure 6.9. Comparison of finite beam A-scan of Class I reflectivity estimated, due to a beam with a Gaussian intensity profile, by both simulators when using the same total number of photon packets, equal to 210×10^7.

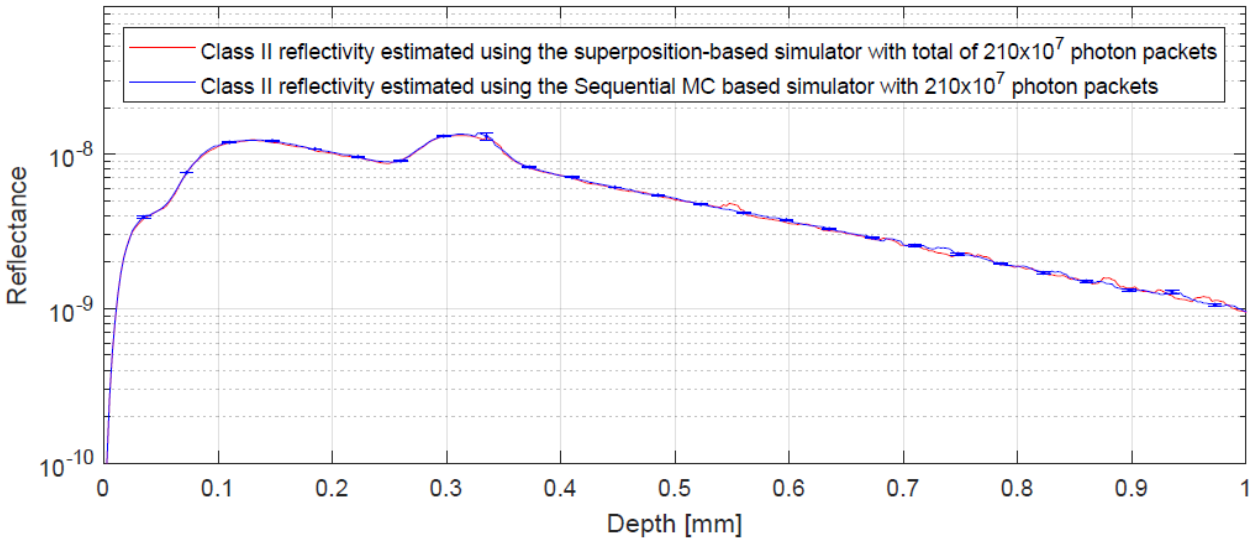

Figure 6.10. Comparison of finite beam A-scan of Class II reflectivity, due to a beam with a Gaussian intensity profile, estimated by both simulators when using the same total number of photon packets, equal to 210×10^7.

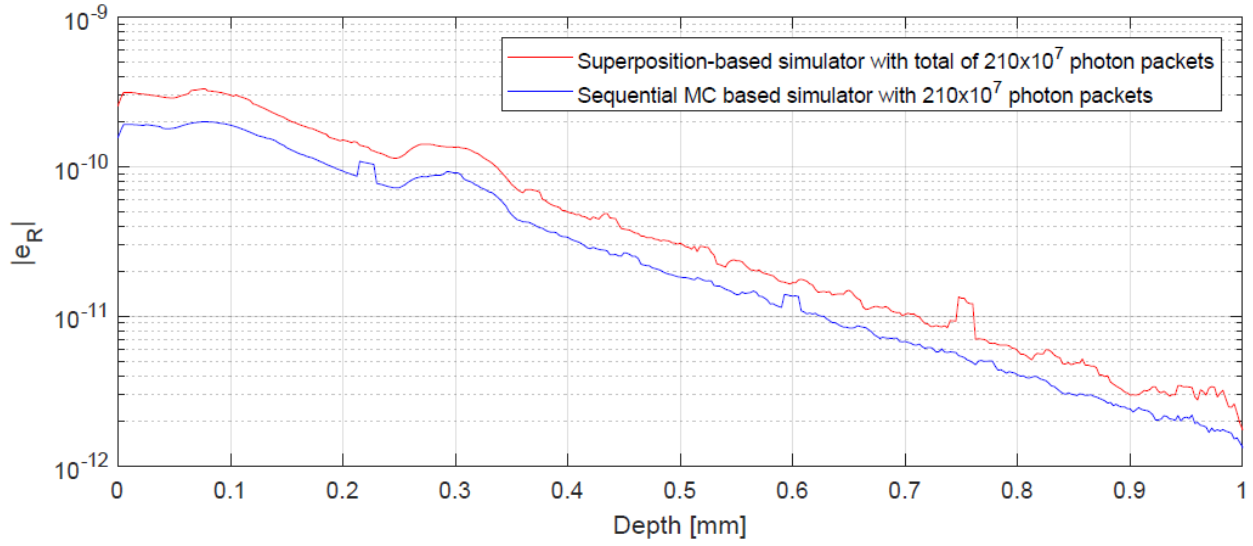

Figure 6.11. Comparison of the error in the estimate of the A-scan of Class I reflectivity obtained by superposition-based simulator (plotted in red), and our Sequential MC based simulator (plotted in blue) when the total number of photon packets are equal (210×10^7 photon packets).

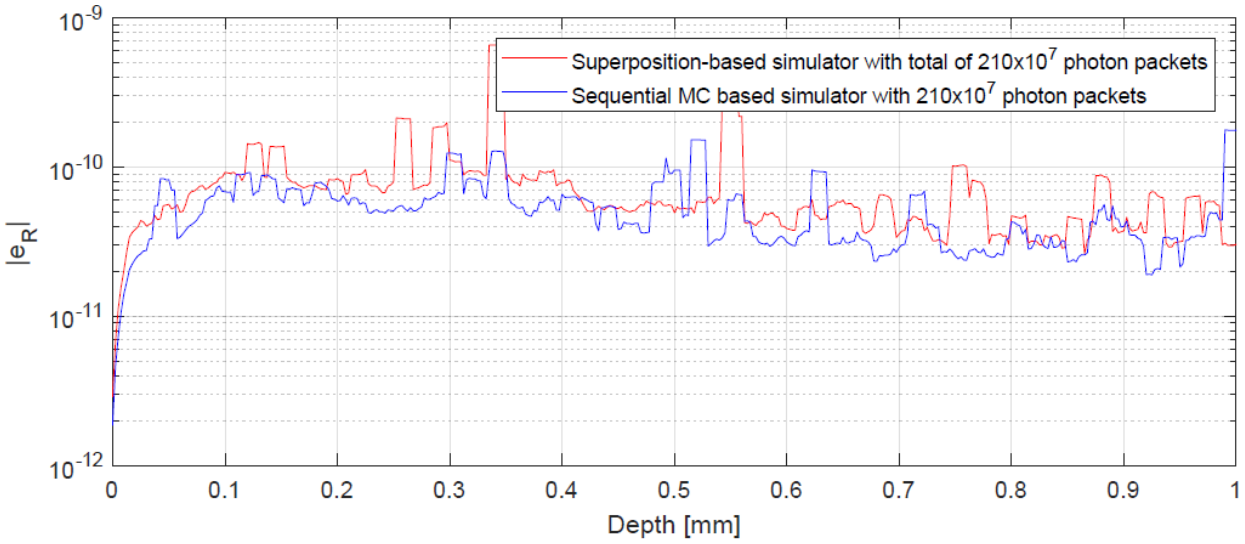

Figure 6.12. Comparison of the error in the estimate of the A-scan of Class II reflectivity obtained by superposition-based simulator (plotted in red), and our Sequential MC based simulator (plotted in blue) when the total number of photon packets are equal (210×10^7 photon packets).

6.4.1.3 Comparison of OCT A-scan when using a finite incident beam and assuming an infinitely-thin incident beam

To demonstrate the importance of using a finite beam OCT simulator we compare the A-scan at the same lateral position, $x = -0.1$ mm, when using a finite incident beam with a Gaussian intensity profile with that when assuming an infinitely-thin incident beam. The finite beam A-scan was simulated using our Sequential MC based simulator, and for both beams the number of photon packets used was 10^7 photon packets.

Figs. (6.13) and (6.14) compare Class I and Class II reflectivity, respectively. Fig. (6.13) shows that there is a significant difference in Class I reflectivity. Fig. (6.14) also shows a significant difference in Class II reflectivity at shallow depths. Figs. (6.15) and (6.16) compare the estimated errors in both cases for Class I and Class II reflectivity respectively. Both figures show that, for equal number of photon packets the error in both cases are approximately equal at all depths.

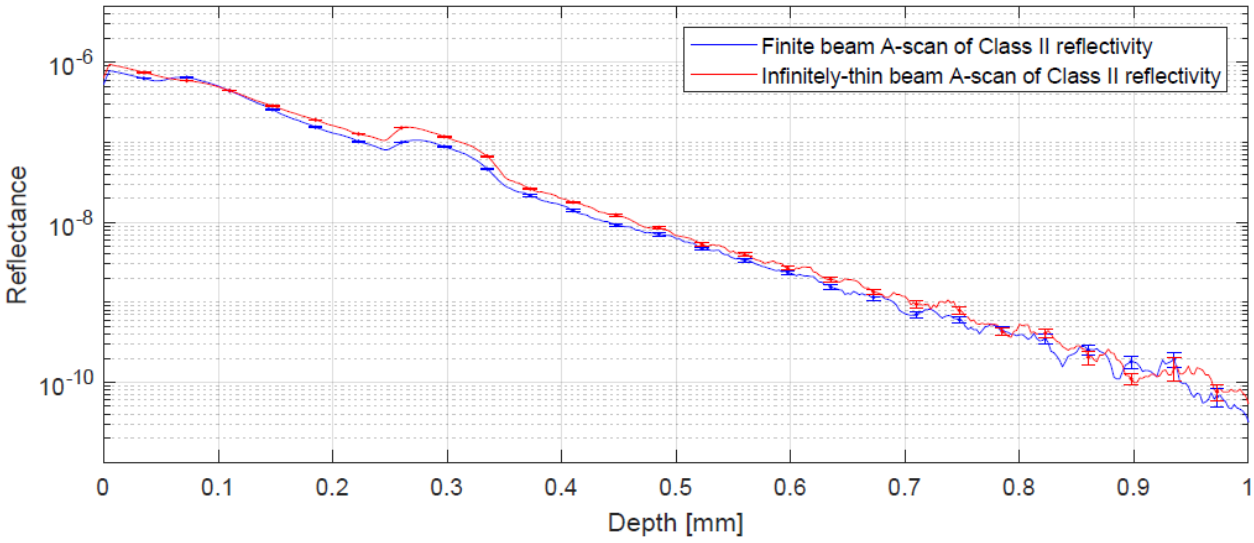

Figure 6.13. Comparison of A-scan of Class I reflectivity when using a finite incident beam with a Gaussian intensity profile (plotted in blue, showing confidence interval at different depths) and when assuming an infinitely-thin incident beam (plotted in blue, showing confidence interval at different depths). A-scan is simulated at $x = -0.1$ mm, in both cases the number of photon packets used was 10^7.

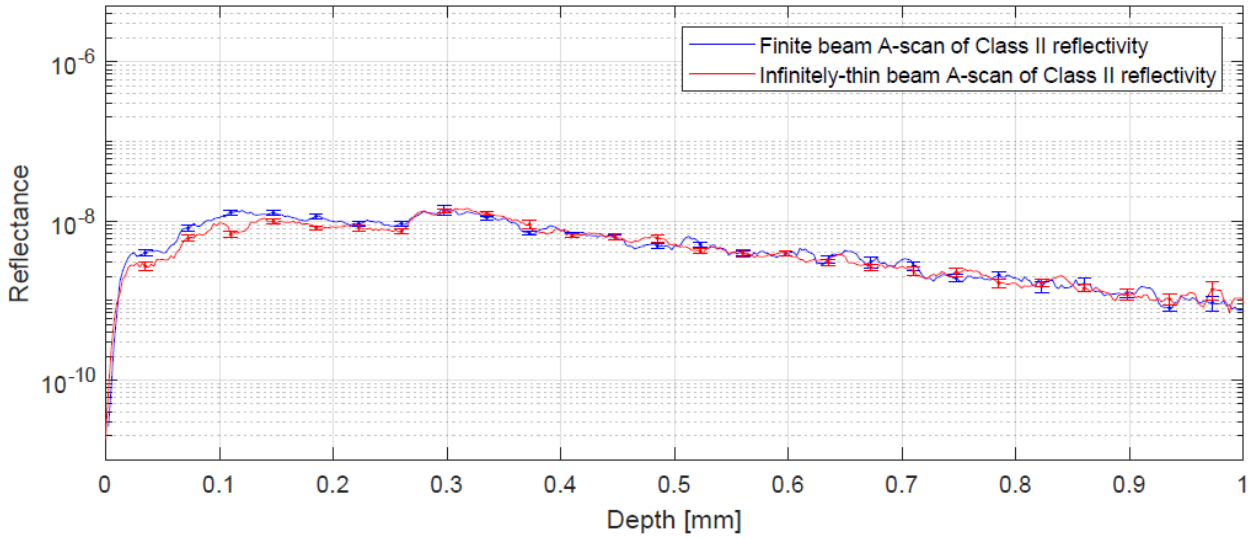

Figure 6.14. Comparison of A-scan of Class II reflectivity when using a finite incident beam with a Gaussian intensity profile (plotted in blue, showing confidence interval at different depths) and when assuming an infinitely-thin incident beam (plotted in blue, showing confidence interval at different depths). A-scan is simulated at $x = -0.1$ mm, in both cases the number of photon packets used was 10^7.

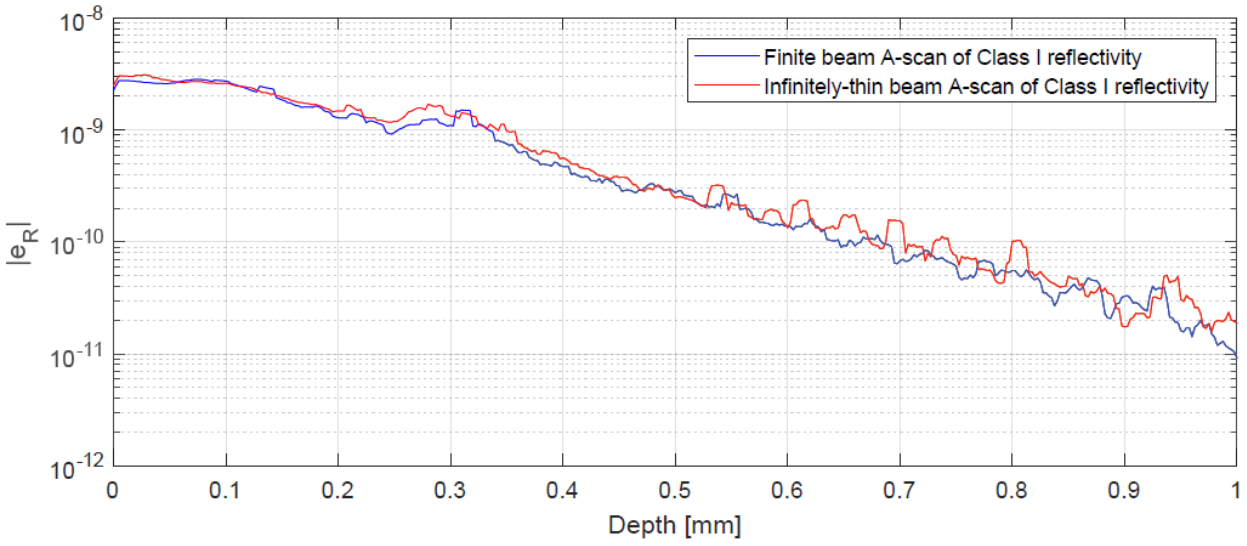

Figure 6.15. Comparison of the error in the estimate of the A-scan of Class I reflectivity when using a finite incident beam with a Gaussian intensity profile (plotted in blue) and when assuming an infinitely-thin incident beam (plotted in red). Finite beam A-scan was simulated using our Sequential MC based simulator. A-scan is simulated at $x = -0.1$ mm, in both cases the number of photon packets used was 10^7.

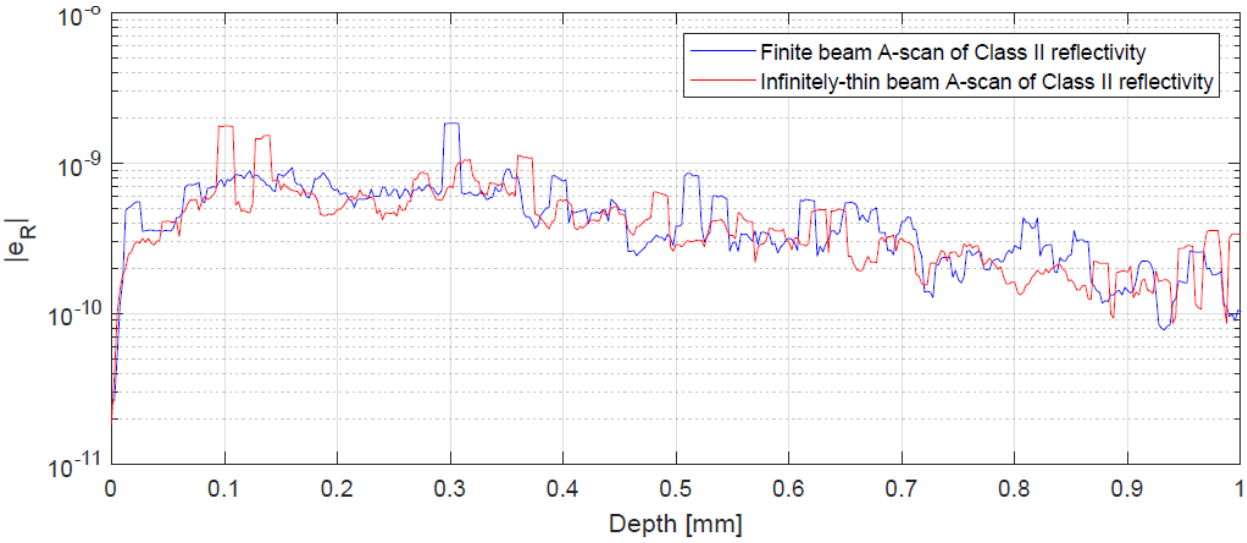

Figure 6.16. Comparison of the error in the estimate of the A-scan of Class II reflectivity when using a finite incident beam with a Gaussian intensity profile (plotted in blue) and when assuming an infinitely-thin incident beam (plotted in red). Finite beam A-scan was simulated using our Sequential MC based simulator. A-scan is simulated at $x = -0.1$ mm, in both cases the number of photon packets used was 10^7.

6.4.1.4 Finite beam B-scan simulation using our Sequential MC based simulator

Finally, we present the simulated reflectivity-based B-scan OCT images, due to finite incident beams with a Gaussian intensity profile, obtained using our Sequential MC based OCT simulator. Figs. (6.17) and (6.18) show the simulated Class I and Class II reflectivity-based B-scan OCT images, respectively. The simulation was done by obtaining 500 equidistant A-scans, each using 10^7 photon packets, along the X-axis from $x = -0.15$ mm to $x = 0.15$ mm.

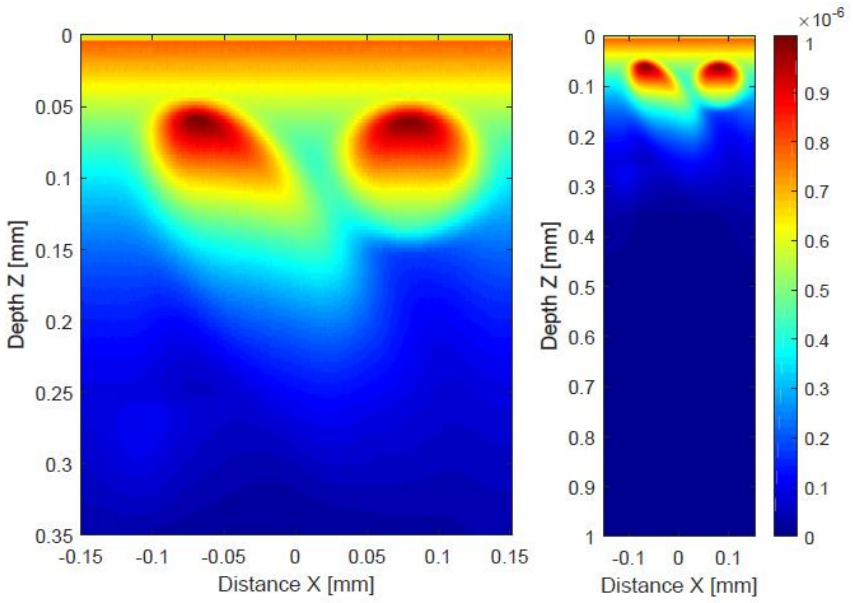

Figure 6.17. Simulated Class I reflectivity-based B-scan OCT images of a slab containing an Ellipsoid and two spheres, when using finite incident beams with a Gaussian intensity profile. Class I B-scan OCT image (right), along with its enlarged version (left), generated by our Sequential MC based finite beam OCT simulator. The surface of the medium is in the XY-plane, i.e., $z = 0$.

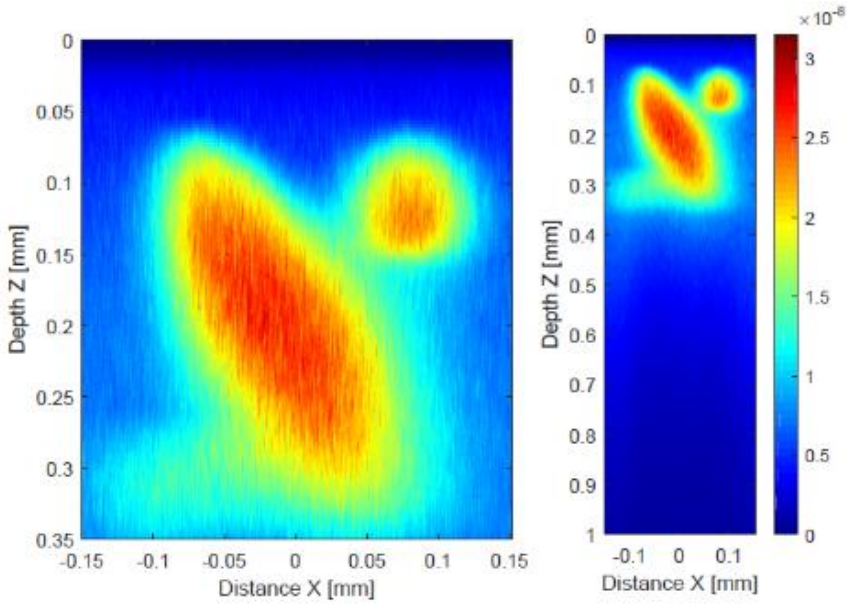

Figure 6.18. Simulated Class II reflectivity-based B-scan OCT images of a slab containing an Ellipsoid and two spheres, when using finite incident beams with a Gaussian intensity profile. Class II B-scan OCT image (right), along with its enlarged version (left), generated by our Sequential MC based finite beam OCT simulator. The surface of the medium is in the XY-plane, i.e., $z = 0$.

As shown in Fig. (6.17) the magnitude of Class I signal gets smaller as the depth in the medium increase. This is what we expect in actual OCT systems, the reason behind that is the low probability of single backscattering at a higher depth. Fig. (6.18) shows that Class II signal has high magnitude inside the objects, this is due to their high scattering coefficients.

6.4.2 Simulation Case 2

The medium consists of a slab containing a tri-axial ellipsoid; its abstract view is shown in Fig. (6.19). The slab is extended for 3 mm in X and Y directions and 0.4 mm in the Z direction. The tri-axial ellipsoid is centered at the position (0.0, 0.0, 0.2) mm. The three vectors representing the axes of the ellipsoid are given by $v_1 = [0.2, 0, 0]^T$ mm, $v_2 = [0, 0.1, 0]^T$ mm, and $v_3 = [0, 0, 0.1]^T$ mm.

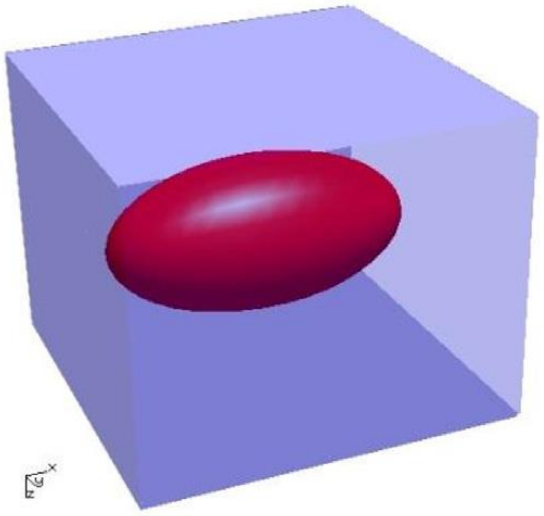

Figure 6.19. Abstract view of the medium: a slab containing an Ellipsoid

The tetrahedron mesh of the medium contains a total of 1275 vertices and 6673 tetrahedrons; it was generated by NETGEN [50]. Fig. (6.20) shows the tetrahedron mesh. The optical properties of the medium are shown in Table (6.2).

Table 6.2. Optical parameters of the medium: a slab containing an Ellipsoid

	'μ_a' (cm^{-1}) Absorption coefficient	'μ_s' (cm^{-1}) Scattering coefficient	'g' Anisotropy factor	'n' Refractive index
Slab	1.5	60	0.9	1
Ellipsoid	3	120	0.9	1

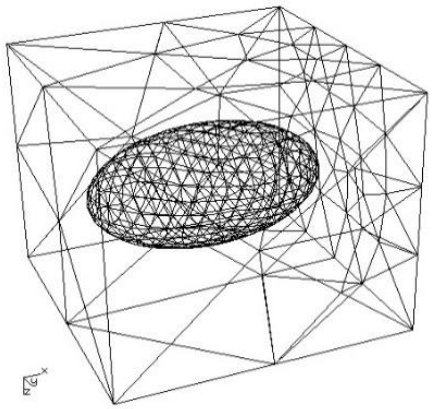

Figure 6.20. Tetrahedron mesh of the medium: a slab containing an Ellipsoid

6.4.2.1 Validation of our finite beam simulator with a superposition-based simulator

We simulate an A-scan at an arbitrary lateral position, $x = 0$, due to a finite incident beam with a Gaussian intensity profile. The number of photon packets simulated at each quadrature node is $N_g = 10^7$. When using the superposition-based simulator the A-scan converged after using 14 quadrature nodes (h_{max} = 20 μm), as shown in Fig. (6.21).

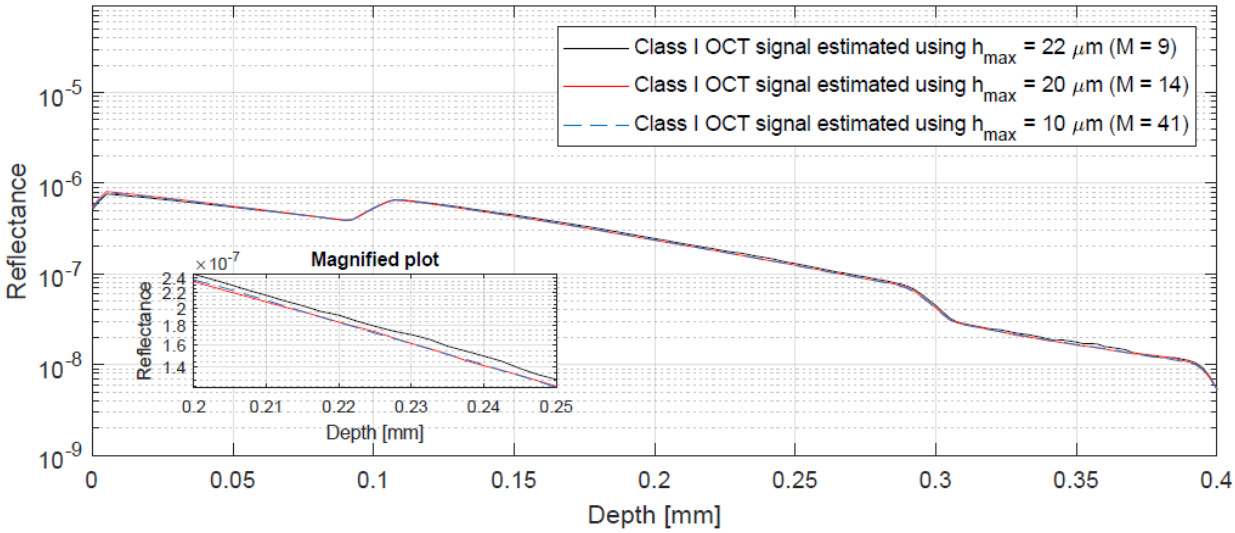

Figure 6.21. Class I signal A-scan, at the lateral position $x = 0$, due to a finite incident beam with a Gaussian intensity profile, obtained using the superposition-based simulator with different number of quadrature nodes (M).

Figs. (6.22) and (6.23) show the A-scan of Class I and Class II reflectivity, respectively, estimated using the superposition-based simulator (with 14 quadrature nodes, total of 14×10^7 photon packets) and our Sequential MC based simulator (with 10^7 photon packets). The figures show that the results of both simulators are in agreement.

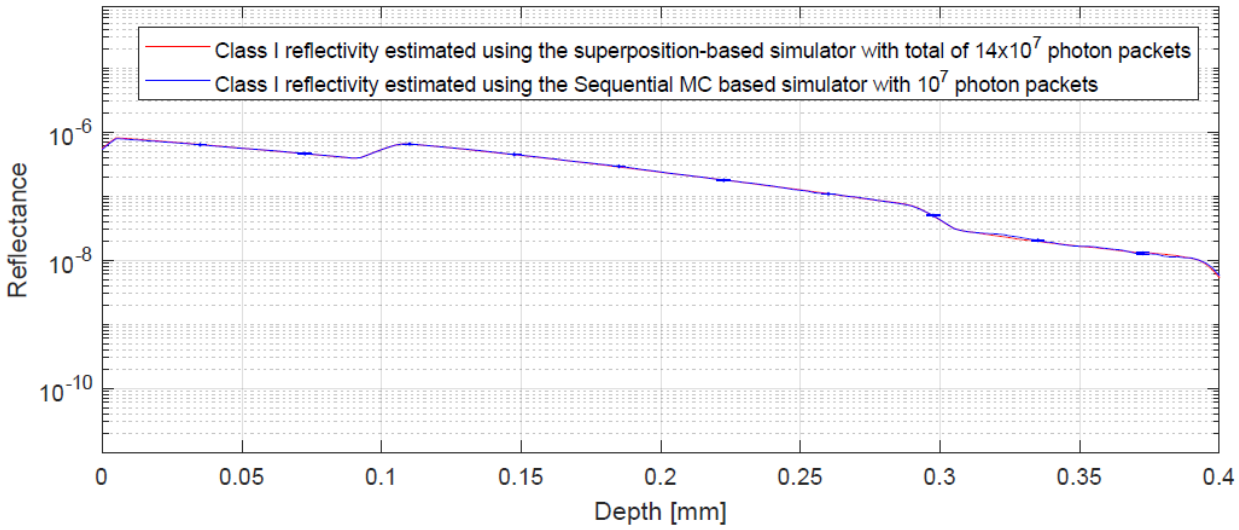

Figure 6.22. Comparison of finite beam A-scan of Class I reflectivity estimated using: superposition-based simulator with a total of 14×10^7 photon packets (14 quadrature nodes, plotted in red), and our Sequential MC based simulator with 10^7 photon packets (plotted in blue, showing confidence interval at different depths).

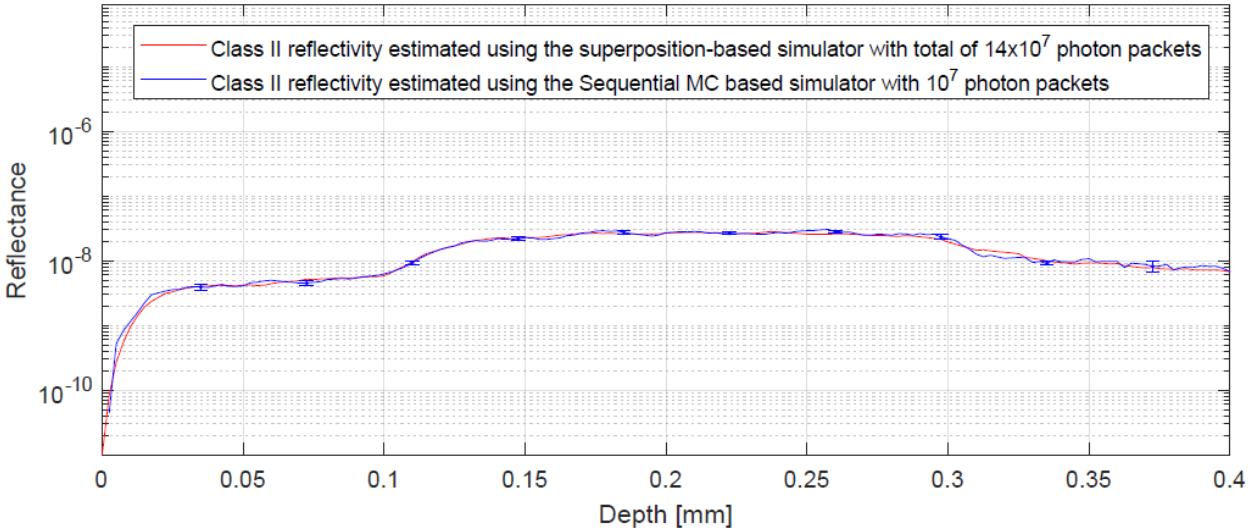

Figure 6.23. Comparison of finite beam A-scan of Class II reflectivity estimated using: superposition-based simulator with a total of 14×10^7 photon packets (14 quadrature nodes, plotted in red), and our Sequential MC based simulator with 10^7 photon packets (plotted in blue, showing confidence interval at different depths).

6.4.2.2 Error comparison and analysis between our simulator and the superposition-based simulator

We compare the errors of both simulators for the A-scan simulated above. We assume that the quadrature error is negligible when using 14 quadrature nodes (as shown in Fig. 6.21). We estimate the error of the superposition-based simulator using Eq. (6.46). Figs. (6.24) and (6.25) compare the errors from both simulators for Class I and Class II reflectivity, respectively. The number of photon packets used by the superposition-based simulator was 14 times more than those used by our Sequential MC based simulator.

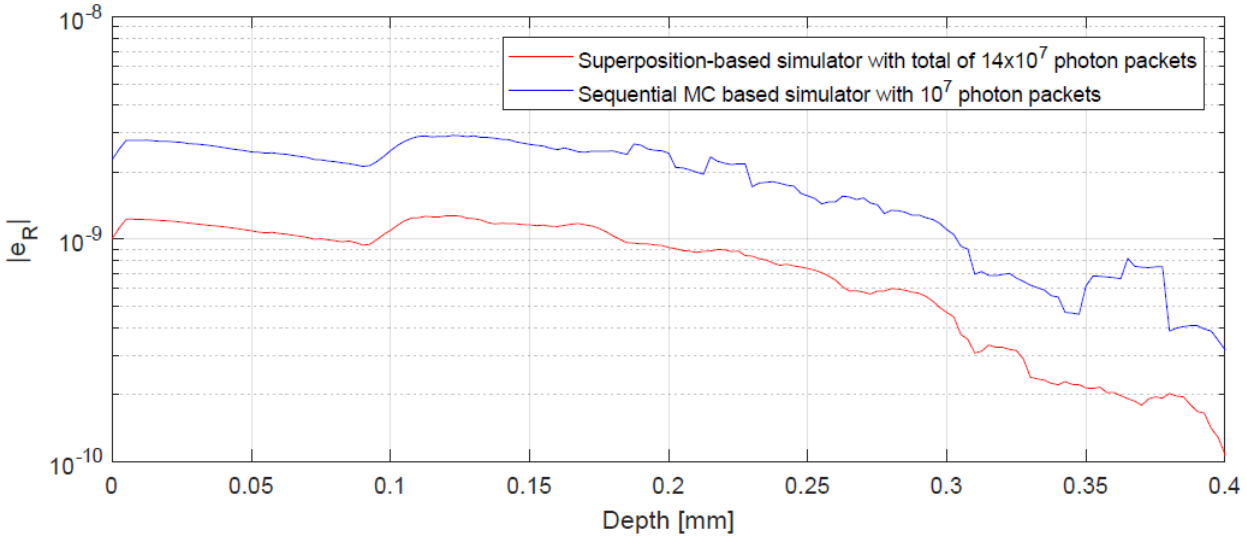

Figure 6.24. Comparison of error in the estimate of Class I reflectivity estimated using: superposition-based simulator with a total of 14×10^7 photon packets (14 quadrature nodes, plotted in red), and our Sequential MC based simulator with 10^7 photon packets (plotted in blue)

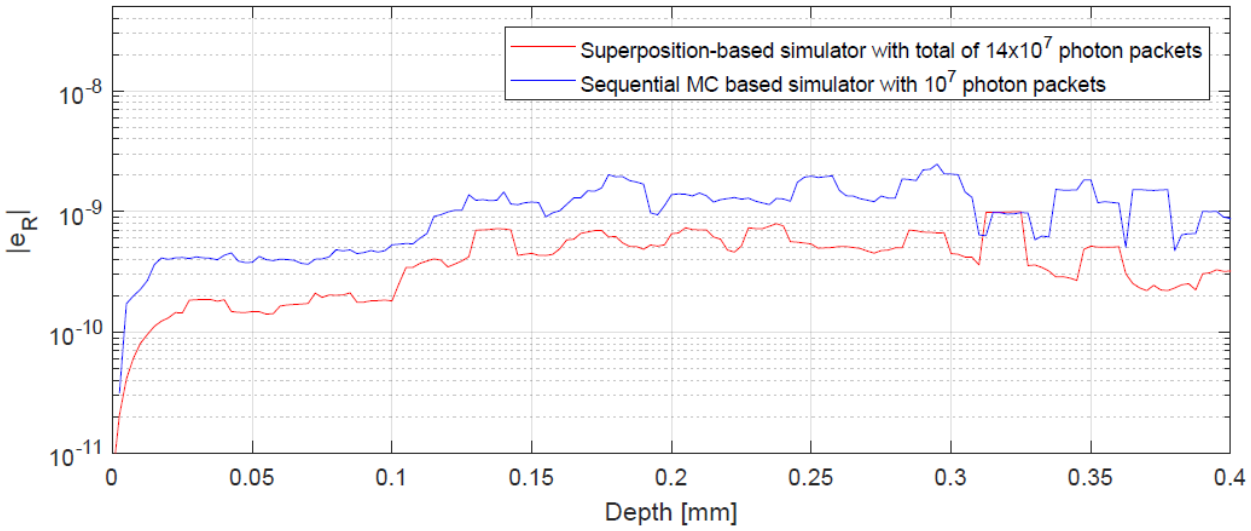

Figure 6.25. Comparison of error in the estimate of Class II reflectivity estimated using: superposition-based simulator with a total of 14×10^7 photon packets (14 quadrature nodes, plotted in red), and our Sequential MC based simulator with 10^7 photon packets (plotted in blue)

To compare the two simulators error at comparable computational cost, we reran our simulator to simulate the same A-scan with $N = 14\times10^7$, which is equal to the total number of photon packets used by the superposition based simulator. Figs. (6.26) and (6.27) compare the estimated errors from both simulators, for Class I and Class II reflectivity respectively, when the number of photon packets are the same (14×10^7 photon packets).

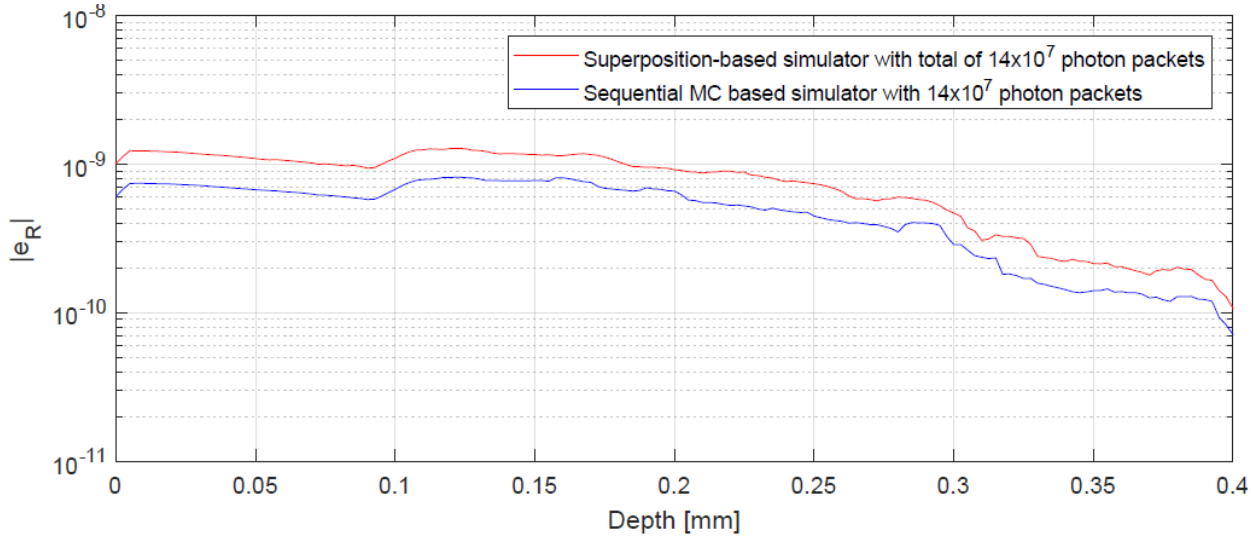

Figure 6.26. Comparison of the error in the estimate of the A-scan of Class I reflectivity obtained by superposition-based simulator (plotted in red), and our Sequential MC based simulator (plotted in blue) when the total number of photon packets are equal (14×10^7 photon packets).

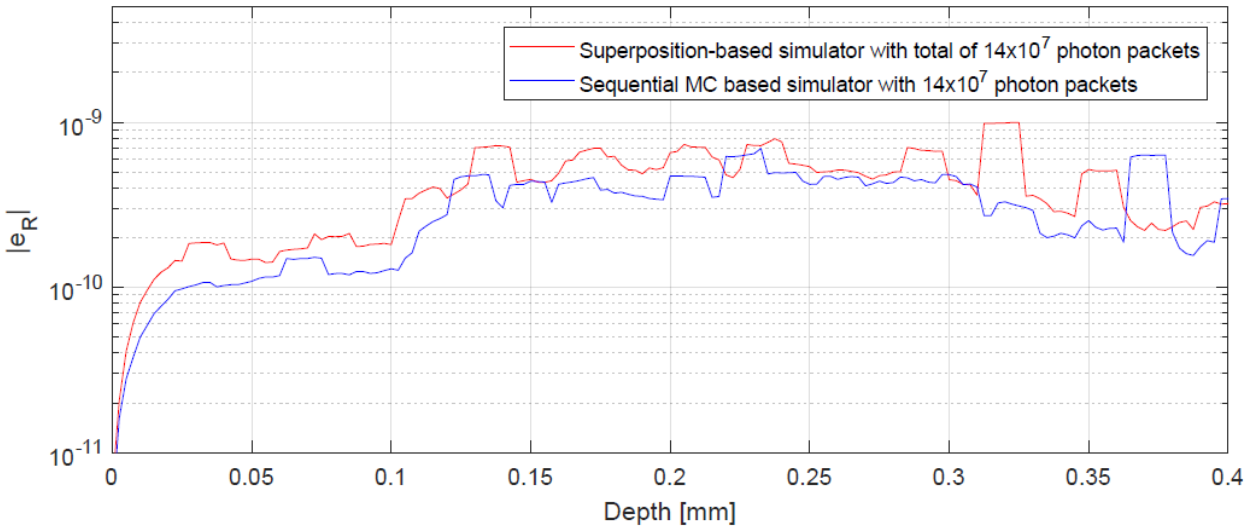

Figure 6.27. Comparison of the error in the estimate of the A-scan of Class II reflectivity obtained by superposition-based simulator (plotted in red), and our Sequential MC based simulator (plotted in blue) when the total number of photon packets are equal (14×10^7 photon packets).

6.4.2.3 Comparison of OCT A-scan when using a finite incident beam and assuming an infinitely-thin incident beam

We compare an A-scan, at an arbitrary lateral position, $x = 0$, due to a finite incident beam having a Gaussian intensity profile with the A-scan due to an infinitely-thin incident beam. For both beams, the number of photon packets used to simulate the A-scan was 10^7. The finite beam A-scan was obtained using the Sequential MC based simulator. Figs. (6.28) and (6.29) compare Class I and Class II reflectivity respectively. Figs. (6.30) and (6.31) compare the estimated errors for Class I and Class II reflectivity respectively.

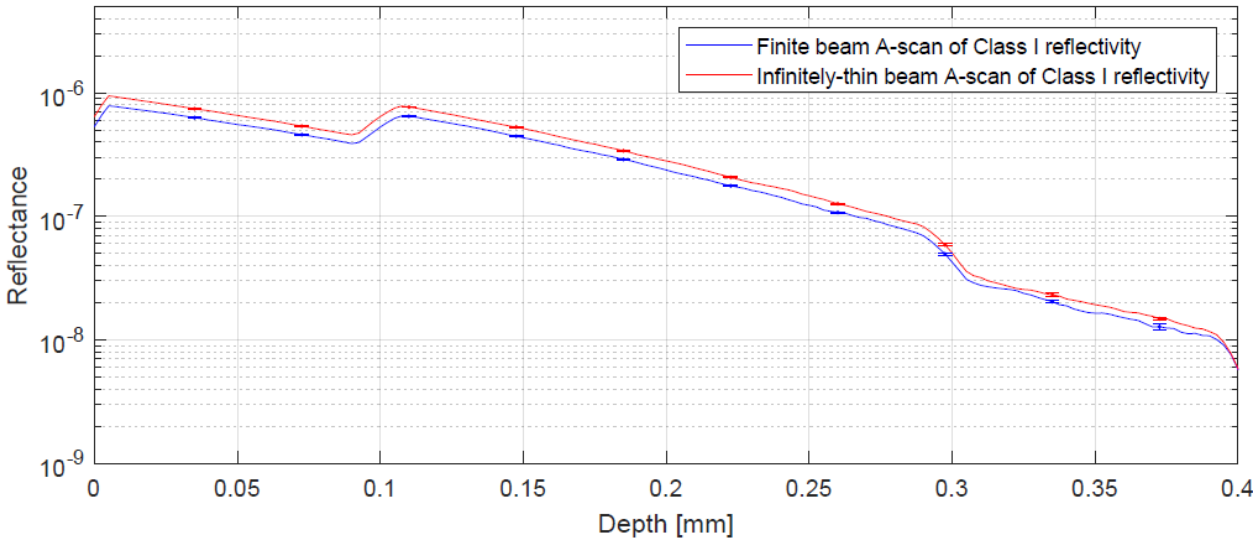

Figure 6.28. Comparison of A-scan of Class I reflectivity when using a finite incident beam with a Gaussian intensity profile (plotted in blue, showing confidence interval at different depths) and when assuming an infinitely-thin incident beam (plotted in red, showing confidence interval at different depths). A-scan is simulated at arbitrary lateral position, $x = 0$, in both cases the number of photon packets used was 10^7.

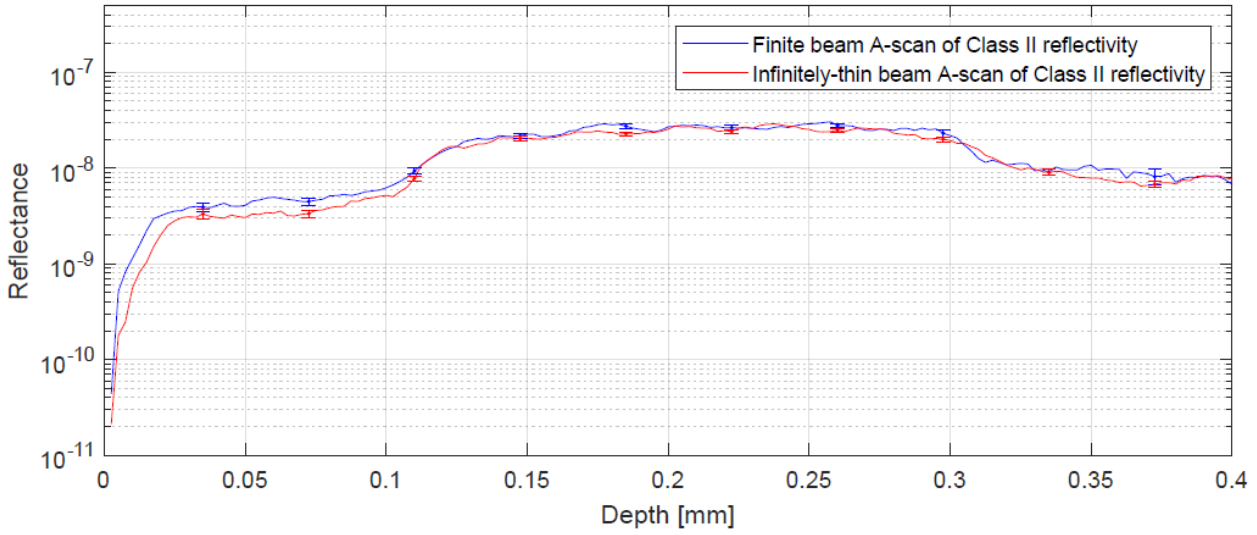

Figure 6.29. Comparison of A-scan of Class II reflectivity when using a finite incident beam with a Gaussian intensity profile (plotted in blue, showing confidence interval at different depths) and when assuming an infinitely-thin incident beam (plotted in red, showing confidence interval at different depths). A-scan is simulated at arbitrary lateral position, $x = 0$, in both cases the number of photon packets used was 10^7.

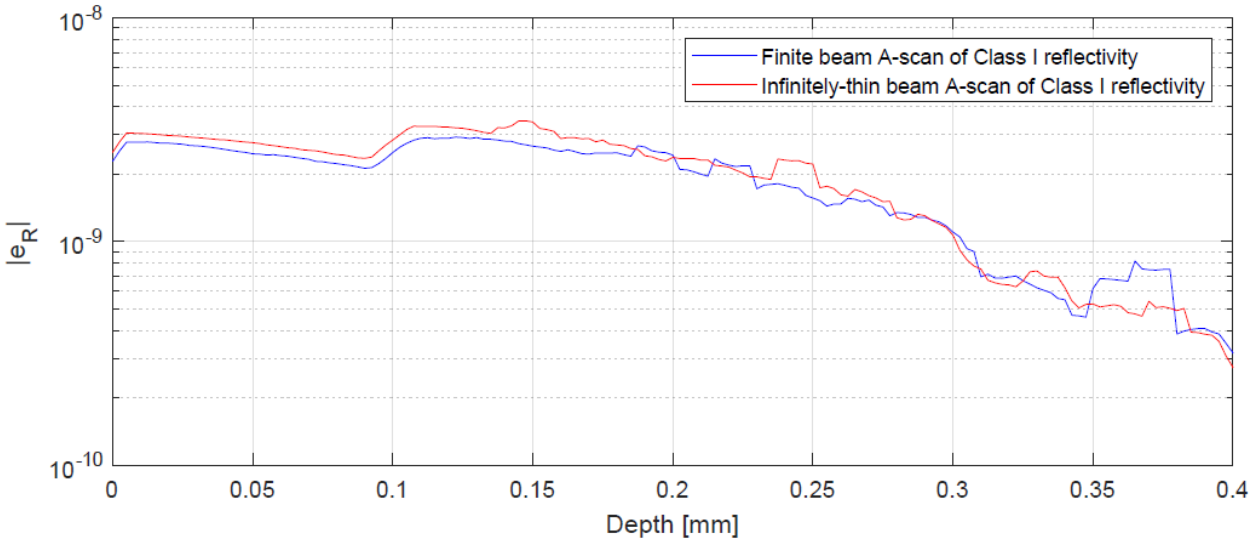

Figure 6.30. Comparison of the error in the estimate of the A-scan of Class I reflectivity when using a finite incident beam with a Gaussian intensity profile (plotted in blue) and when assuming an infinitely-thin incident beam (plotted in red). Finite beam A-scan was simulated using our Sequential MC based simulator. A-scan is simulated at arbitrary lateral position, $x = 0$, in both cases the number of photon packets used was 10^7.

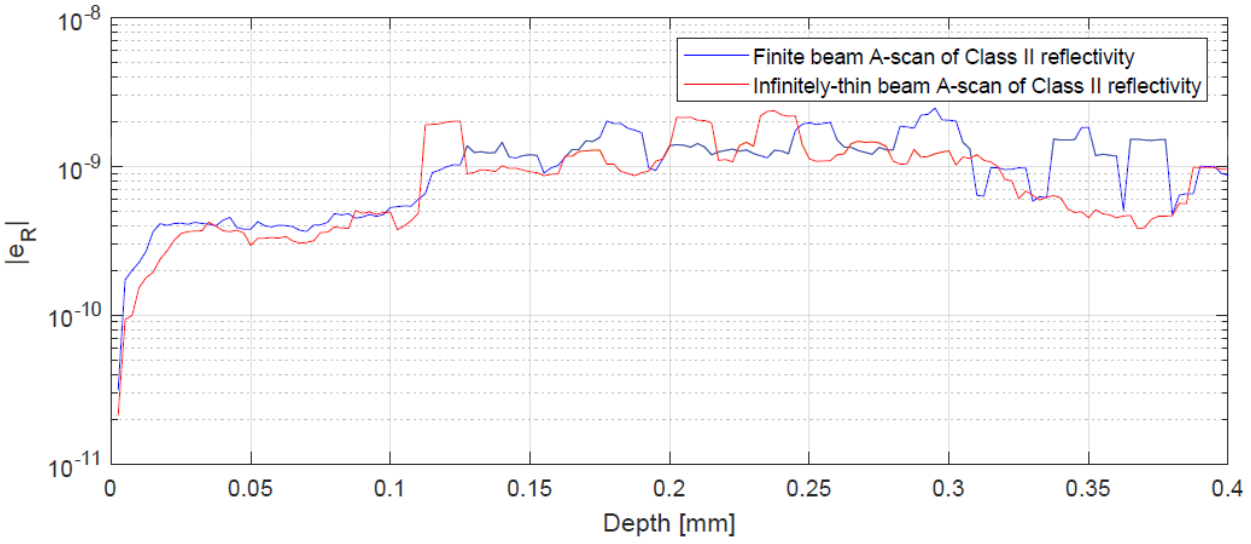

Figure 6.31. Comparison of the error in the estimate of the A-scan of Class II reflectivity when using a finite incident beam with a Gaussian intensity profile (plotted in blue) and when assuming an infinitely-thin incident beam (plotted in red). Finite beam A-scan was simulated using our Sequential MC based simulator. A-scan is simulated at arbitrary lateral position, $x = 0$, in both cases the number of photon packets used was 10^7.

6.4.2.4 Finite beam B-scan simulation using our Sequential MC based simulator

Finally, Figs. (6.32) and (6.33) show the simulated Class I and Class II reflectivity-based B-scan OCT images, respectively, due to finite incident beams with a Gaussian intensity profile. The simulated B-scan was constructed of 100 equidistant A-scans, each simulated using 10^7 photon packets, along the X-axis from $x = -0.25$ mm to $x = 0.25$ mm.

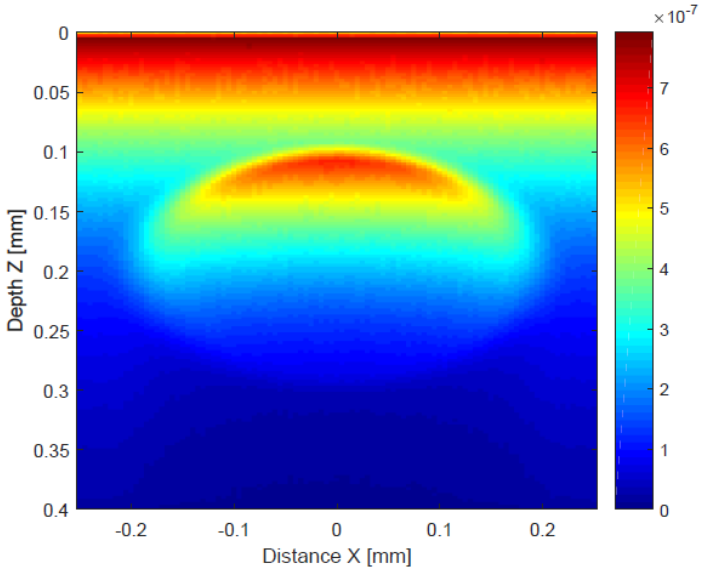

Figure 6.32. Class I reflectivity-based B-scan OCT images of a slab containing an Ellipsoid, when using finite incident beams with a Gaussian intensity profile. B-scan was simulated using our Sequential MC based finite beam OCT simulator. The surface of the medium is in the XY-plane, i.e., $z = 0$.

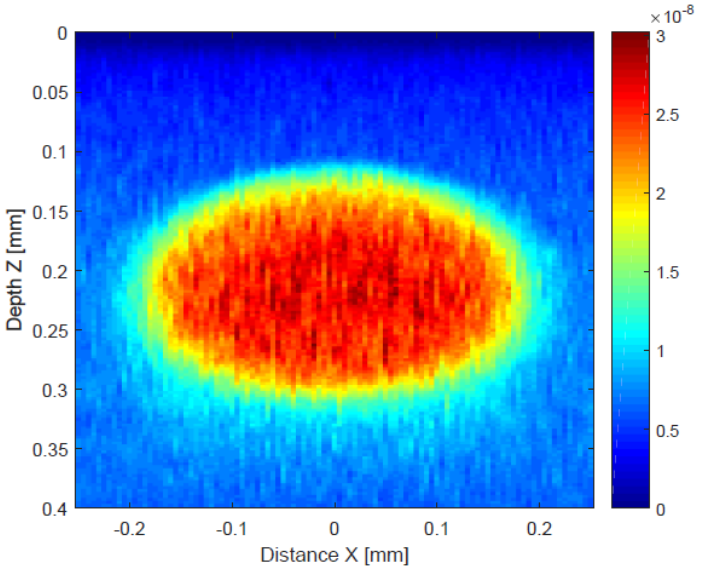

Figure 6.33. Class II reflectivity-based B-scan OCT images of a slab containing an Ellipsoid, when using finite incident beams with a Gaussian intensity profile. B-scan was simulated using our Sequential MC based finite beam OCT simulator. The surface of the medium is in the XY-plane, i.e., $z = 0$.

Chapter 7

Conclusions and suggested future work

7.1 Conclusions

We present the derivation of the linear integral form of the RTE, for homogeneous turbid media, form its integro-differential form. We present a solution of the RTE using Sequential MC methods. We established the correspondence between the Sequential MC solution of the RTE for homogeneous media and the MC simulation method for light transport.

We developed and implemented a finite-beam OCT simulator for inhomogeneous turbid media with arbitrary boundaries between regions of different optical properties based on the Sequential MC solution of the RTE. Our simulator is implemented on GPUs using NVIDIA's CUDA architecture and extensions of the C language. We validated our simulator with an equivalent simulator that represents the finite beam OCT signal (A-scan) with the superposition of the OCT signals (A-scans) due to infinitely-thin beams covering the beam area. We compared the accuracy and computational cost of both simulators, showing that our simulator has superior performance. We presented the simulated finite beam reflectivity-based B-scan OCT images for two inhomogeneous arbitrarily shaped media due to finite incident beams with a Gaussian intensity profile.

7.2 Suggested future work

As future work, we suggest using other advanced MC methods, such as reversible jump Markov Chain Monte Carlo and advanced particle filtering techniques, to simulate light

propagation in tissue more efficiently. One thing that can make our simulator more physically realistic is to include light polarization. Our OCT simulator simulates time domain OCT system, but it can be extended to simulate swept source OCT systems.

References

[1] D. Huang, E. A. Swanson, C. P. Lin, J. S. Schuman, W. G. Stinson, W. Chang, M. R. Hee, T. Flotte, K. Gregory, C. A. Puliafito, and A. Et, "Optical coherence tomography," Science, vol. 254, no. 5035, pp. 1178–1181, Nov. 1991.

[2] Brezinski, M. E. (2006). Optical coherence tomography: principles and applications. Elsevier.

[3] W. Drexler , J.G. Fujimoto , Optical Coherence Tomography, Springer, 2008.

[4] D.P. Popescu , C. Flueraru , Y. Mao , S. Chang , J. Disano , S.S. Sherif , M.G. Sowa, Optical coherence tomography: fundamental principles, instrumental designs and biomedical applications, Biophys. Rev. 3 (3) (2011) 155–169.

[5] W. Drexler , U. Morgner , R.K. Ghanta , F.X. Kärtner , J.S. Schuman , J.G. Fujimoto, Ultrahigh-resolution ophthalmic optical coherence tomography, Nat. Med. 7 (4) (2001) 502–507.

[6] Sattler EC, Kästle R, Welzel J. Optical coherence tomography in dermatology. Journal of biomedical optics. 2013 Jan;18(6):061224.

[7] Hsieh YS, Ho YC, Lee SY, Chuang CC, Tsai JC, Lin KF, Sun CW. Dental optical coherence tomography. Sensors. 2013 Jul 12;13(7):8928-49.

[8] Saleh, B. E., Teich, M. C., & Saleh, B. E. (1991). Fundamentals of photonics (Vol. 22). New York: Wiley.

[9] Lorenzo, J. R. (2012). Principles of diffuse light propagation: light propagation in tissues with applications in biology and medicine. World Scientific.

[10] Born, M., & Wolf, E. (1999). Principles of Optics, 7th (expanded) ed. Cambridge U. Press, Cambridge, UK, 890.

[11] Chew, W. C. (1995). Waves and fields in inhomogeneous media. IEEE press.

[12] Patterson, M. S., Wilson, B. C., & Wyman, D. R. (1991). The propagation of optical radiation in tissue I. Models of radiation transport and their application. Lasers in Medical Science, 6(2), 155-168.

[13] Carter, L. L., & Cashwell, E. D. (1975). Particle-transport simulation with the Monte Carlo method (No. TID--26607). Los Alamos Scientific Lab..

[14] Wang, L. V., & Wu, H. I. (2012). Biomedical optics: principles and imaging. John Wiley & Sons.

[15] Dunn, W. L., & Shultis, J. K. (2011). Exploring monte carlo methods. Elsevier.

[16] Fujimoto, J. G., Pitris, C., Boppart, S. A., & Brezinski, M. E. (2000). Optical coherence tomography: an emerging technology for biomedical imaging and optical biopsy. Neoplasia (New York, NY), 2(1-2), 9.

[17] Siavash Malektaji. "Monte Carlo simulation of optical coherence tomography of media with arbitrary spatial distributions." M.Sc. thesis, University of Manitoba, Canada, 2014.

[18] B. Wilson , G. Adam , A Monte Carlo model for the absorption and flux distributions of light in tissue, Med. Phys. 10 (6) (1983) 824–830.

[19] L. H. Wang et al., “MCML-Monte-Carlo modeling of light transport in multilayered tissues,” Comput. Meth. Prog. Bio. 47(2), 131–146 (1995).

[20] E. Alerstam, W. Lo, T. Han, J. Rose, S. Andersson-Engels, L. Lilge, "Next-generation acceleration and code optimization for light transport in turbid media using GPUs," Biomed. Opt. Express, 1(2), 658–675 (2010).

[21] Shen H, Wang G. A tetrahedron-based inhomogeneous Monte Carlo optical simulator. Physics in Medicine & Biology. 2010 Jan 20;55(4):947.

[22] Fang Q. Mesh-based Monte Carlo method using fast ray-tracing in Plücker coordinates. Biomedical optics express. 2010 Aug 2;1(1):165-75.

[23] N. Ren, J. Liang, X. Qu, J. Li, B. Lu, J. Tian, "GPU-based Monte Carlo simulation for light propagation in complex heterogeneous tissues," Opt.Express, 18(7), 6811–6823 (2010).

[24] Ren S, Chen X, Wang H, Qu X, Wang G, Liang J, Tian J. Molecular optical simulation environment (MOSE): a platform for the simulation of light propagation in turbid media. PloS one. 2013 Apr 8;8(4):e61304.

[25] Q. Fang, D. Boas, "Monte Carlo simulation of photon migration in 3D turbid media accelerated by graphics processing units," Opt. Express, 17(22), 20178–20190 (2009).

[26] D.J. Smithies, T. Lindmo, Z. Chen, J.S. Nelson, T.E. Milner , Signal attenuation and localization in optical coherence tomography studied by Monte Carlo simulation, Phys. Med. Biol. 43 (10) (1998) 3025–3044.

[27] G. Yao, L. Wang, Monte Carlo simulation of an optical coherence tomography signal in homogeneous turbid media, Phys. Med. Biol. 44 (9) (1999) 2307.

[28] I.T. Lima, A. Kalra, S.S. Sherif, Improved importance sampling for Monte Carlo simulation of time-domain optical coherence tomography, Biomed. Opt. Ex- press 2 (5) (2011) 1069–1081.

[29] I.T. Lima, A. Kalra, H.E. Hernandez-Figueroa, S.S. Sherif, Fast calculation of multipath diffusive reflectance in optical coherence tomography, Biomed. Opt. Ex- press 3 (4) (2012) 692–700.

[30] M.Y. Kirillin, E. Alarousu, T. Fabritius, R.A. Myllylä, A.V. Priezzhev, Visualization of paper structure by optical coherence tomography: Monte Carlo simulations and experimental study, J. Opt. Soc. Rapid 2 (2007) 07031.

[31] V. Periyasamy, M. Pramanik, Monte Carlo simulation of light transport in turbid medium with embedded object—spherical, cylindrical, ellipsoidal, or cuboidal objects embedded within multilayered tissues, J. Biomed. Opt. 19 (4) (2014) 045003-045003.

[32] V. Periyasamy, M. Pramanik, Importance sampling-based Monte Carlo simulation of time-domain optical coherence tomography with embedded objects, Appl. Opt. 55 (11) (2016) 2921–2929.

[33] S. Malektaji, I.T. Lima Jr., S.S. Sherif, Monte Carlo simulation of optical coherence tomography for turbid media with arbitrary spatial distributions, J. Biomed. Opt. 19 (4) (2014) 046001.

[34] S. Malektaji, I. Lima, M. Escobar I. and S. Sherif, "Massively parallel simulator of optical coherence tomography of inhomogeneous turbid media," Computer Methods and Programs in Biomedicine 150, 97-105 (2017).

[35] Mauricio R. Escobar I.. "Massively parallel simulator of optical coherence tomography of inhomogeneous media." M.Sc. thesis, University of Manitoba, Canada, 2015.

[36] Kalos, M. H., & Whitlock, P. A. (1986). Monte Carlo methods, vol. 1. Basics: Wiley & Sons, New York, USA.

[37] G. Marsaglia, Random number generators, J. Mod. Appl. Stat. Meth. 2 (1) (2003) 2–13.

[38] E. Alerstam, W.C.Y. Lo, T.D. Han, J. Rose, S. Andersson-Engels, L. Lilge, Next-generation acceleration and code optimization for light transport in turbid media using GPUs, Biomed. Opt. Express 1 (2) (2010) 658–675.

[39] Doucet, A., Johansen, A. M., & Tadić, V. B. (2010). On solving integral equations using Markov chain Monte Carlo methods. Applied Mathematics and Computation, 216(10), 2869-2880.

[40] Farnoosh, R., & Ebrahimi, M. (2008). Monte Carlo method for solving Fredholm integral equations of the second kind. Applied Mathematics and Computation, 195(1), 309-315.

[41] Dimov, I. T., Dimov, T. T., & Gurov, T. V. (1998). A new iterative Monte Carlo approach for inverse matrix problem. Journal of Computational and Applied Mathematics, 92(1), 15-35.

[42] Duderstadt, J. J., & Martin, W. R. (1979). Transport theory. Transport theory., by Duderstadt, JJ; Martin, WR. Chichester (UK): John Wiley & Sons, 10+ 613 p.

[43] Doucet, A., & Johansen, A. M. (2009). A tutorial on particle filtering and smoothing: Fifteen years later. Handbook of nonlinear filtering, 12(656-704), 3.

[44] Levy, D. (2010). Introduction to numerical analysis. Department of Mathematics and Center for Scientific Computation and Mathematical Modeling, CSCAMM, University of Maryland.

[45] Dahlquist, G., & Björck, Å. (2008). Chapter 5: Numerical Integration. Numerical methods in scientific computing, 1.

[46] Baird, D. C., & Simpson, J. A. (1962). Experimentation: an introduction to measurement theory and experimental design. Physics Today, 15, 65.

[47] Leon-Garcia, A. (2017). Chapter 5: Pairs of Random Variables. Probability, statistics, and random processes for electrical engineering.

[48] Mahler, H. C., & Dean, C. G. (2001). Chapter 8: Credibility In Foundations of Casualty Actuarial Science. Casualty Actuarial Society (pp. 525-526). ISBN 978–0–96247-622-8.

[49] Moon, T. K., & Stirling, W. C. (2000). Mathematical methods and algorithms for signal processing (Vol. 1). Upper Saddle River, NJ: Prentice hall.

[50] Schöberl, J. (1997). NETGEN An advancing front 2D/3D-mesh generator based on abstract rules. Computing and visualization in science, 1(1), 41-52.